(46)

Pair Production of W Bosons in Electron Positron Annihilation

by

Steven C. Nahn

B.S., University of Wisconsin (1991)

Submitted to the Department of Physics
in partial fulfillment of the requirements for the degree of

Doctor of Philosophy

at the

MASSACHUSETTS INSTITUTE OF TECHNOLOGY

February 1998

Author .....
Department of Physics
January 28 1997

Certified by .....
Peter H Fisher
Professor of Physics
Thesis Supervisor

Accepted by .....
George F Koster
Chairman, Departmental Committee on Graduate Students

Pair Production of W Bosons in Electron Positron Annihilation

by

Steven C. Nahn

Submitted to the Department of Physics
on January 28 1997, in partial fulfillment of the
requirements for the degree of
Doctor of Philosophy

Abstract

In the last decade, the precision of the Standard Model has increased dramatically, due to studies of electroweak physics at the LEP collider. From the beginning of 1996, the LEP collider has operated at or above the threshold for W boson pair production, providing a new set of tests for the Standard Model. The L3 detector collected 21 pb^{-1} of data at center of mass energies of 161 and 172 GeV in 1996, which is analyzed to measure the W-pair production cross sections, the W branching ratios, and the W mass, with the results:

$$\begin{aligned}
\sigma_{\mathrm{WW}}(\sqrt{s} = 161\ \mathrm{GeV}) &= 2.87^{+0.80}_{-0.69} \pm 0.08\ \mathrm{pb} \\
\sigma_{\mathrm{WW}}(\sqrt{s} = 172\ \mathrm{GeV}) &= 12.12^{+1.43}_{-1.34} \pm 0.18\ \mathrm{pb} \\
B(\mathrm{W} \to qq) &= 63.6^{+3.8}_{-4.0} \pm 0.4\ \% \\
B(\mathrm{W} \to \ell\nu) &= 12.1^{+1.3}_{-1.3} \pm 0.2\ \% \\
\mathrm{M_W} &= 80.75 \pm 0.29\ \mathrm{GeV}
\end{aligned}$$

all of which are consistent with the Standard Model. In particular, the mass measurement agrees with $\mathrm{M_W} = 80.352 \pm 0.033$, the W mass from a determination [1] using the precise predictions of the Standard Model.

Thesis Supervisor: Peter H Fisher
Title: Professor of Physics

Contents

1 Introduction **6**

2 Theory of W-pair observables **10**

2.1 Production Cross Sections 10

2.2 W Decay Branching Ratios 11

2.3 W Mass 14

3 LEP and the L3 Detector **17**

3.1 LEP 17

3.2 The L3 detector 18

3.3 Data Samples 21

4 Selection of W-pair events **23**

4.1 Selection of $qqe\nu$ final states 25

4.2 Selection of $qq\mu\nu$ final states 26

4.3 Selection of $qq\tau\nu$ final states 27

4.4 Selection of $\ell\nu\ell\nu$ final states 27

4.5 Selection of $qqqq$ final states 28

4.6 Cross Efficiencies and Systematic Errors 31

5 Measurement of Cross Sections and Branching Ratios **33**

5.1 Non W-pair Interference 33

5.2 Cross section and branching ratios determinations 33

5.3 Results 36

6 Measurement of W Mass **38**

6.1 Threshold method 38

6.2 Direct Reconstruction 41

6.3 Results 46

7 Summary **48**

7.1 Challenging the Standard Model 48

7.2 Future Prospects 50

8 Acknowlegdements **52**

1 Introduction

The origin of the modern theory of weak interactions dates to 1932, when Fermi proposed a charged current interaction similar to Quantum Electrodynamics (QED) but with a smaller coupling constant (thus "weak") to explain beta decay rates [2]. Fermi's theory was moderately successful in interpreting and predicting weak phenomena (for instance inverse beta decay $\bar{\nu}_e + p \rightarrow e^+ + n$, discovered soon after [3]), but was missing one major ingredient, Parity violation. In 1956 Yang and Lee pointed out that Parity conservation had no experimental support [4], and C.S. Wu *et al.* showed Parity was not conserved in the weak interactions [5]. Wu's discovery led to many experiments which established the "Vector - Axial (V-A)" vector current structure of the weak interaction. The major consequence of this structure is that only chirally left-handed fermions, which correspond to negative helicity fermions in the massless limit, interact weakly. For this reason, since neutrinos are apparently massless and only interact weakly, all detectable neutrinos must have negative helicity. With this major modification, Fermi's theory successfully explained all weak interaction data at the low energies of that time.

However, from early on in this period it was known that this theory is not complete, as it is not renormalizable [6] . This means that the theory predicts observables such as the neutrino-nucleon cross sections which grow with the center of mass energy ($\sqrt{s}$), violating unitarity constraints at $\sqrt{s} \approx 700$ GeV. The correct theory must incorporate all features of low energy theory *and* be renormalizable. The formulation of a theory which satisfies these requirements took place in the 1960s, first by Glashow [7], and later independently by Salam [8] and Weinberg [9]. This theory, based on gauge symmetries and renormalization, unifies the electromagnetic and weak interactions and is so successful that it is the cornerstone of what is now known as the Standard Model.

In a nutshell[1], the electroweak sector of the Standard Model starts with the as-

[1]The features of the Standard Model have been elucidated in great detail. Full descriptions can be found in, for instance, [10] or [11].

sumption that a triplet of Yang-Mills gauge bosons under the weak isospin symmetry group $SU_L(2)$ mediates the weak interaction, where the L signifies that only the left-handed fermions couple to the gauge bosons. The insertion of the boson propagator solves the unitarity problem and provides a prediction of the W boson mass (M_W)

$$M_W^2 \sim \frac{g_w^2}{G_F}$$

where g_w is the coupling between the fermions and the weak bosons. Implicit in the assumption of a triplet of bosons is the existence of a neutral weak boson W^3, with the same quantum numbers as the photon. Starting with a QED-like boson B which couples to hypercharge Y, the appropriate combination of weak isospin and electric charge, the electromagnetic and the weak interactions are unified by mixing the hypercharge boson and the neutral weak boson with mixing angle θ_W to form the physical states, the A (photon) and Z bosons:

$$\begin{pmatrix} A \\ Z \end{pmatrix} = \begin{bmatrix} \cos\theta_W & \sin\theta_W \\ -\sin\theta_W & \cos\theta_W \end{bmatrix} \begin{pmatrix} B \\ W^3 \end{pmatrix}$$

This also unifies the electromagnetic and weak couplings by the relationship $g_w = e \sin\theta_W$ which allows the prediction of the mass from the couplings and mixing angle:

$$M_W^2 = \frac{\alpha\pi}{\sqrt{2} G_F \sin^2\theta_W}$$

However, normal mass terms for Yang-Mills bosons are not gauge invariant, yet, the short range nature of the weak interactions require that the weak bosons have mass. The weak bosons acquire mass in a gauge invariant way via the Higgs mechanism [12], which introduces a neutral scalar field coupling to the weak bosons, endowing them with mass while leaving the photon massless.

The establishment of the theory was gradual, starting with its proof of renormalizability in 1971 by 't Hooft [13]. Further acceptance came with the first observation of weak neutral currents by the Gargamelle collaboration in 1973 [14]. A key experi-

	M_W [GeV]	m_t [GeV]	m_H [GeV]
Direct	80.356 ± 0.125	175 ± 6	> 66
Indirect	$80.278 \pm 0.049^{+0.013}_{-0.024}$	176^{+8+17}_{-7-19}	< 550 (95% C.L.)

Table 1: Direct and indirect determinations of the W boson mass M_W and the top quark mass m_t, and limits on the Higgs mass m_H [1]. The last uncertainty in the indirect determinations is from varying the Higgs mass from 60 to 1000 GeV.

ment by Prescott *et al.* [15] in 1978 was the measurement of $\sin\theta_W$ via the interference between the neutral current diagrams of Z and photon exchange. This experiment utilized the difference in couplings between right and left handed fermions, measuring an asymmetry in particle production yields as a function of the incoming helicity state in electron-nucleon scattering. With α and G_F known, the measurements of $\sin\theta_W$ from Prescott and ν experiments at CERN pinpointed the weak boson mass, allowing tuning of the beam energy for direct searches. In the early 80s, the UA1 and UA2 collaborations at the CERN Sp$\bar{p}$S collider observed the weak bosons [16–19] near the predicted masses in proton-antiproton collisions at $\sqrt{s} = 630$ GeV via the detection of lepton pairs with high invariant mass, thus solidifying the validity of the electroweak theory.

Since the discovery of the Z and W bosons, electroweak experiments have refined the Standard Model to ever increasing precision without revealing signs of breakdown. The electroweak sector is defined by three inputs from experiment, typically α, G_F, and either $\sin\theta_W$ or the Z boson mass M_Z. These inputs are known to a precision of $\sim 10^{-3}$ or better, making the model sensitive to higher order corrections dependent on interactions with virtual particles whose properties are less well measured, such as the top quark and the W boson. Using these higher order corrections, the masses of the top quark and W boson can be indirectly determined, and compared to the measured values from the Tevatron [20–24] (Table 1). The agreement then permits the next step, which is to place constraints on the contributions from unmeasured sources, such as the Higgs boson or physics beyond the Standard Model.

This thesis constitutes the initial foray into the next set of tests for electroweak

theory, using pair production of W bosons. In 1996, the center of mass energy in the LEP collider was pushed above the threshold for W-pair production $\sqrt{s} = 2M_W$, allowing for the first time the detailed study of W-pair observables. In this first phase of LEPII, the L3 detector recorded 11.0 pb^{-1} and 10.25 pb^{-1} of e^+e^- annihilation data at center of mass energies of 161 and 172 GeV, respectively. This data is used to measure the W-pair production cross sections for all final states, the W decay branching ratios, and the W mass.

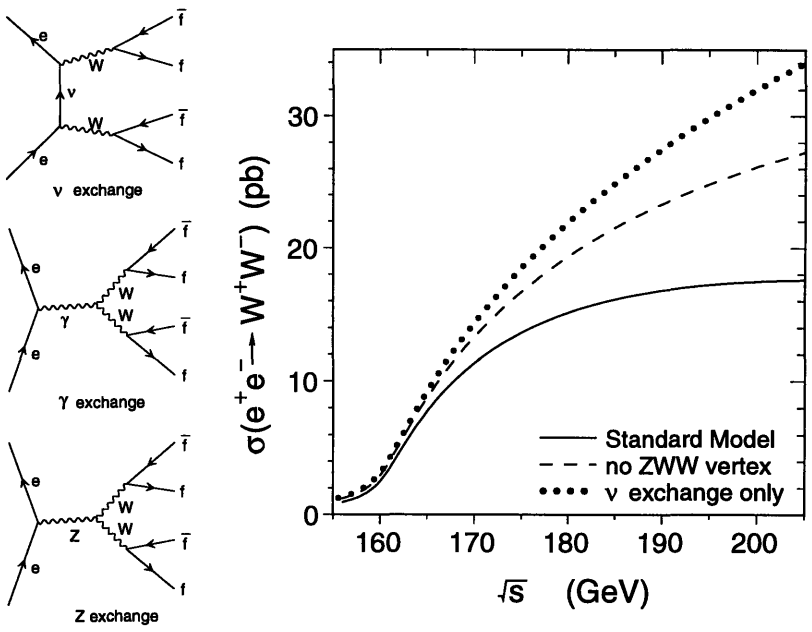

Figure 1: Lowest order diagrams and cross section for $e^+e^- \rightarrow WW$ as a function of $\sqrt{s}$, showing the gauge cancellations when all diagrams are included.

2 Theory of W-pair observables

2.1 Production Cross Sections

The elegance of electroweak theory is fully evident in the lowest order calculations of W-pair production. There are three diagrams which contribute at lowest order, the s channel photon and Z exchange and the t channel neutrino exchange. The photon and Z exchange diagrams contain trilinear gauge boson vertices, a direct consequence of the non-abelian nature of electroweak theory. Seperately, the cross section from each diagram diverges at high energy, but the combination of the three converges to the s^{-1} behavior required by unitarity [25]. Thus the specific trilinear couplings from electroweak theory which arise because of the gauge groups involved automatically keep the theory renormalizable (Fig 1).

The calculation of the lowest order cross section is straightforward, if tedious. However, there are higher order corrections due to virtual and radiative processes, the finite width of the W boson, and interference from other diagrams with the same final state, all of which complicate the calculation sufficiently that an analytical solu-

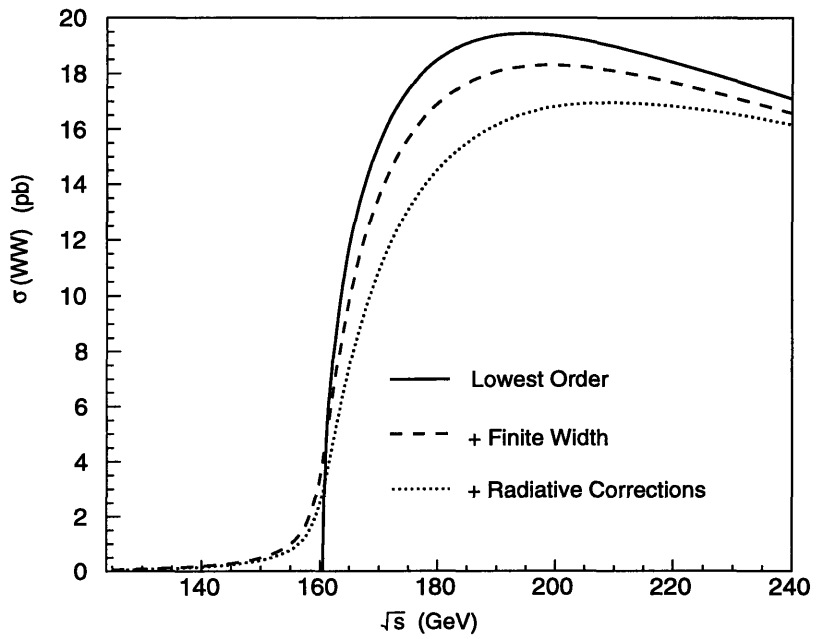

Figure 2: Comparison of lowest order cross section with inclusion of the finite W width and radiative and virtual corrections [26].

tion is intractable, and the job becomes the task of computer integration programs. The effects of these corrections can be large, but are theoretically under control [26]. Radiative corrections and finite width inclusion both simply change the numerical cross sections values (Fig. 2), while in contrast, the inclusion of other diagrams also affects the interpretation of the measurements. As as example, all 18 diagrams contributing to the process $e^+e^- \to e\nu\mu\nu$ are shown in figure 3. The measured cross section, which includes contributions from all diagrams, is dominated by the "doubly resonant" lowest order subset of figure 1, which contains the W-pair production processes. The additional contributions from other diagrams are known [26,27], allowing the interpretation of the measurement in terms of the W-pair processes only.

2.2 W Decay Branching Ratios

The W partial width to final state $f_i f'_j$ is given by [26]:

$$\begin{aligned} \Gamma_{W f_i f'_j} &= N_C^f \Gamma^0 |V_{ij}|^2 f(M_W, m_{f_i}, m_{f'_j}) \\ \Gamma^0 &= \frac{G_F M_W^3}{6\sqrt{2}\pi} \end{aligned}$$

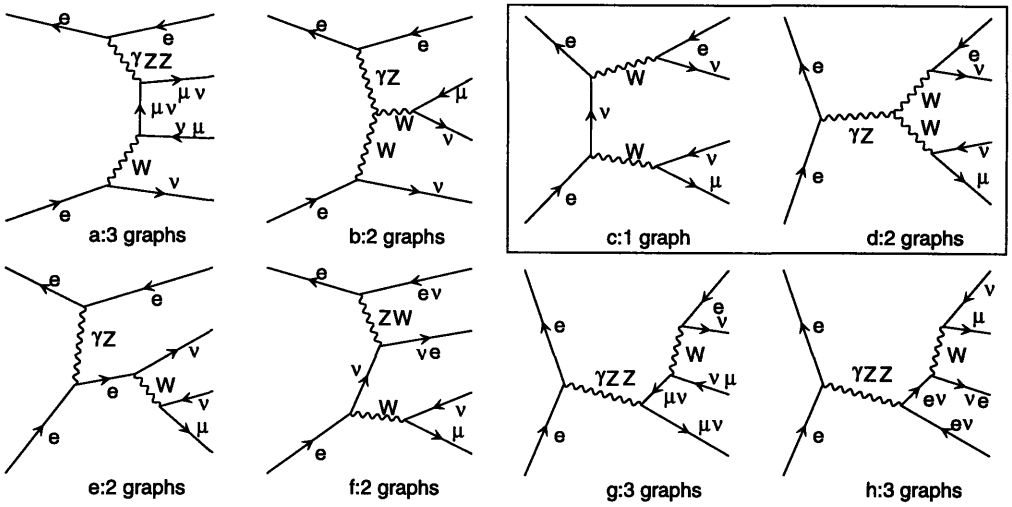

Figure 3: All 18 diagrams for the process $e^+e^- \to e\nu\mu\nu$. Some diagrams are the same except for permutations of boson and/or fermion labels. The diagrams of figure 1 are in the box.

$$f(M_W, m_{f_i}, m_{f'_j}) = \left[1 - \frac{m_{f_i}^2 + m_{f'_j}^2}{2M_W^2} - \frac{(m_{f_i}^2 - m_{f'_j}^2)^2}{2M_W^4}\right] \times \frac{\sqrt{2\left(M_W^2 - (m_{f_i} + m_{f'_j})^2\right)\left(M_W^2 - (m_{f_i} - m_{f'_j})^2\right)}}{M_W^2}$$

where N_C^f is the color factor, m_f the mass of fermion f, and V_{ij} the flavor mixing matrix. The leptonic decay ($N_C^f = 1, V_{ij} = \delta_{ij}$) is theoretically well understood, as it is essentially the charged current interaction that has been studied over the last 70 years, with no QCD or flavor mixing complications. W decays become more interesting when considering hadronic decays, since there the Cabbibo-Kobayashi-Maskawa (CKM) mixing matrix [28] comes into play. The CKM matrix is the mechanism for relating the weak eigenstates to the strong eigenstates for the quarks, conventionally via a rotation of the negatively charged quarks:

$$\begin{pmatrix} d' \\ s' \\ b' \end{pmatrix} = \begin{bmatrix} V_{ud} & V_{us} & V_{ub} \\ V_{cd} & V_{cs} & V_{cb} \\ V_{td} & V_{ts} & V_{tb} \end{bmatrix} \begin{pmatrix} d \\ s \\ b \end{pmatrix}$$

where the primed (unprimed) quarks are the weak (strong) eigenstates. The CKM matrix not only codifies the flavor changing hadronic weak decays, but also with a complex entry becomes a possible source of CP violation, one of the few open questions left in the Standard Model.

The mass of the W is much larger than that of any of its decay products, so to a good approximation the phase space factor $f(\mathrm{M_W}, m_{f_i}, m_{f'_j}) = 1$ for all decay channels. This makes the partial widths independent of the final state such that the calculation of the W branching ratios amounts to counting up the different final states a W can decay into, taking into account the color factor:

$$\mathrm{W} \longrightarrow \begin{pmatrix} \nu_\mathrm{e} \\ \mathrm{e} \end{pmatrix}, \begin{pmatrix} \nu_\mu \\ \mu \end{pmatrix}, \begin{pmatrix} \nu_\tau \\ \tau \end{pmatrix}, \begin{pmatrix} u \\ d' \end{pmatrix}, \begin{pmatrix} c \\ s' \end{pmatrix}$$

$$\Gamma_{\mathrm{Tot}} = \Gamma^0 [\ 1 + 1 + 1 + 3 + 3\ ]$$

$$B(\mathrm{W} \to qq) \equiv \frac{\Gamma_{ud'}+\Gamma_{cs'}}{\Gamma_{\mathrm{Tot}}} = \frac{2}{3}$$

$$B(\mathrm{W} \to \ell\nu) \equiv \frac{\Gamma_{e\nu}+\Gamma_{\mu\nu}+\Gamma_{\tau\nu}}{\Gamma_{\mathrm{Tot}}} = \frac{1}{3}$$

where $B(\mathrm{W} \to qq)$ is the branching ratio to hadrons and $B(\mathrm{W} \to \ell\nu)$ is the branching ratio to leptons. The assumption that the W couples with equal strength to each lepton family is known as lepton universality, and can be tested using W-pair events. Including higher order effects from stong interactions in the final state changes the above relationships only by a few percent (Fig. 5). Within the Standard Model, the CKM matrix elements and the hadronic branching ratio are related by:

$$\sum_{i=u,c;j=d,s,b} |V_{ij}|^2 = \left(\frac{1}{1+\alpha_s/\pi}\right) \cdot \frac{B(\mathrm{W}\to qq)}{1-B(\mathrm{W}\to qq)}$$

The measurement is most sensitive to the diagonal matrix elements V_{ud} and V_{cs}, of which the least well known is $V_{cs} = 1.01 \pm 0.18$ [29]. Taking the other matrix elements as known, a measurement of the W branching ratio to hadrons can be interpreted as a measurement of $|V_{cs}|$, assuming no unknown W decay modes.

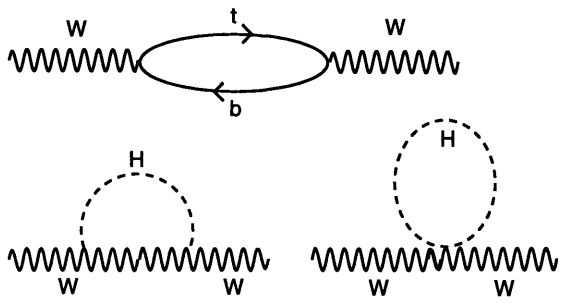

Figure 4: Diagrams linking M_W to m_t and m_H.

m_H[GeV]	Δm_H [GeV]	
	ΔM_W = 25 MeV	ΔM_W = 50 MeV
100	+86,-54	+140,-72
300	+196,-126	+323,-168

Table 2: Extracted constraints on m_H from electroweak fits, as a function of m_H and the experimental error on the W mass ΔM_W, for m_t= 180 $\pm$ 5 GeV [33].

2.3 W Mass

The origin of electroweak boson mass is the Higgs mechanism, which ties together the masses according to the equation

$$\frac{M_W^2}{M_Z^2 \cos^2\theta_W} = \rho$$

with $\rho = 1$ for the minimal Higgs model. Therefore, at lowest order the measurements of M_Z and $\sin^2\theta_W$ from LEP and SLD provide an indirect determination of M_W, to be compared with direct determinations. Beyond lowest order, the above relationship is modified by virtual corrections to the self-energies of the electroweak bosons [30–32]. The diagrams in figure 4 introduce quadratic top mass (m_t) dependence and logrithmic Higgs mass (m_H) dependence, which are used with the current best experimental values as constraints to fit for the best set of values of (M_W,m_t,m_H) [1]. As a consequence, a higher accuracy measurement of M_W, with m_t taken from the Tevatron experiments [21–24], can further constrain m_H (Table 2), thus pointing to the Higgs boson mass for future colliders.

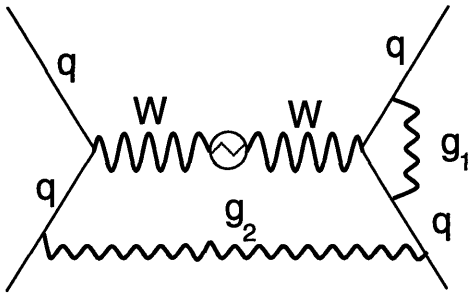

Figure 5: Cartoon of strong interactions in the final state. The interaction via g_1 affects the W width, while the interaction via g_2 affects the W invariant mass.

Theoretically, the origins of and the self-energy corrections to the W mass are well understood. However, there are theoretical complications when trying to measure the mass from *two* hadronically decaying W bosons by reconstructing the invariant masses from the decay quarks momenta, due to final state interactions (FSI). Strong interactions between the final state quarks cause the first complication. The W bosons decay within $\sim$ 0.1 fm of the interaction vertex, smaller than the typical strong interaction scale of 1 fm. The decay quarks can interact both with their partner decay quarks and the decay quarks from the other W, such that the kinematics of the final state quarks do not necessarily reproduce the kinematics of the Ws. Interactions between quarks of different Ws will shift the reconstructed W momenta, thus shifting the reconstructed W invariant masses (Fig. 5). This effect is often called "Color Reconnection" [33, 34].

A second effect called "Bose-Einstein correlation" [35] which acts after hadronization, on the particle level, is similar to Color Reconnection in effect, but has a different origin. Quantum mechanics requires that the final state be symmetric under the exchange of any two identical bosons, following Bose-Einstein statistics. Correlations between identical pions and kaons from different W decays imply that the momenta of the final state particles do not necessarily reflect the momenta of the original Ws, again resulting in shifts of the reconstructed invariant masses.

The magnitude of these effects are model and method dependent, and there is no clearly correct model or method. Survey of the estimates on M_W shifts due to final state interactions, which vary from tens to hundreds of MeV, suggests a reasonable

allowance of 50 MeV for each effect [33]. Further understanding of these phenomena, which now comes from computer simulations implementing a particular model, awaits experimental input to discern which model correctly describes Nature.

3 LEP and the L3 Detector

3.1 LEP

The **L**arge **E**lectron **P**ositron (LEP) collider is a 27 km circumference storage ring outside of Geneva, Switzerland, built for studying electroweak physics via e^+e^- collisions at $\sqrt{s} \sim 100 - 200$ GeV [36, 37]. The first phase of LEP (LEPI) was devoted to studying production and decay of Z bosons at $\sqrt{s} \sim M_Z \pm 3$ GeV, and is chiefly responsible for the high level of precision in the electroweak sector, producing [1]:

$$M_W = 91.1863 \pm 0.0020 \qquad \Gamma_Z = 2.4942 \pm 0.0027 \qquad \sin^2\theta_W = 0.2249 \pm 0.0009$$

Since 1996, the capabilites of the LEP ring have been enhanced by the addition of superconducting accelerating cavities, allowing increases in the center of mass energy and luminosity, ushering in the LEPII era [38, 39].

From the standpoint of W-pair physics, the crucial operating parameters of the LEP ring are the amount of luminosity it delivers and the resolution of the center of mass energy. W-pair production cross sections are roughly three orders of magnitude less than that typical of LEPI Z production, requiring significant increases in luminosity to achieve reasonable statistical error. In contrast, the center of mass energy affects the systematic precision of the measurement due to its extensive use in the selection of W-pair events and the analysis of the W mass. The understanding of the center of mass energy is thus an important part of W-pair physics analyses.

The LEP beam energy (and therefore center of mass energy) is accurately measured by the process of resonant depolarization [40]. Resonant depolarization is a practical application of the following facts:

1. A circulating beam of electrons will polarize due to synchrotron radiation.

2. The spin of a polarized electron moving in a uniform magnetic field will precess, due to the anamolous magnetic moment of the electron, $(g_e - 2)$, according to the BMT equations [41].

The beam energy is related to the precession frequency $f_{\rm prec}$ via the equation:

$$E_{\rm beam} = \left(\frac{m_{\rm e}c^2}{(g_{\rm e}-2)/2}\right)\frac{f_{\rm prec}}{f_{\rm rev}}$$

where the quantity in parenthesis is known to a precision of 3×10^{-7} [42] and the revolution frequency $f_{\rm rev}$ is known to a precision of 3.5×10^{-6} [43], so an accurate measurement of $f_{\rm prec}$ translates to an accurate measure of $E_{\rm beam}$. The measurement of $f_{\rm prec}$ consists of applying a perturbing field with variable frequency to the polarized beam. The effect of the perturbing field on the polarization averages out unless the perturbation frequency precisely matches $f_{\rm prec}$, where instead the beam depolarizes. Thus, the frequency is varied slowly until depolarization occurs, which gives a measure of the beam energy. This technique used at LEPI gives energy resolutions of order 10^{-5} [43].

At higher energies polarizing the beam becomes difficult [44], such that resonant depolarization cannot be directly utilized for energies above some maximum energy $E^{\rm pol}_{\rm max}$, which is less than the beam energy for LEPII. Instead, other systems for measuring beam energy, based on measurements of the LEP bending magnetic field, are coupled to a sophisticated model for time-dependent beam energy behavior, and then calibrated using resonant depolarization between two energies, $E_{\rm beam} = \frac{\rm Mz}{2}$ and $E_{\rm beam} = E^{\rm pol}_{\rm max}$. The value for $E_{\rm beam}$ at physics energies is extrapolated from this calibration, making the energy resolution a function of $E^{\rm pol}_{\rm max}$ and inflating the intrinsic resonant depolarization accuracy by roughly one order of magnitude (Fig. 6).

3.2 The L3 detector

The L3 detector [45] is a general purpose detector designed to measure the energies and momenta of all particles resulting from an e^+e^- collision. It consists of a silicon micro-strip detector, a central tracking chamber, a high-resolution electromagnetic calorimeter composed of Bismuth Germaninum Oxide (BGO) crystals, a

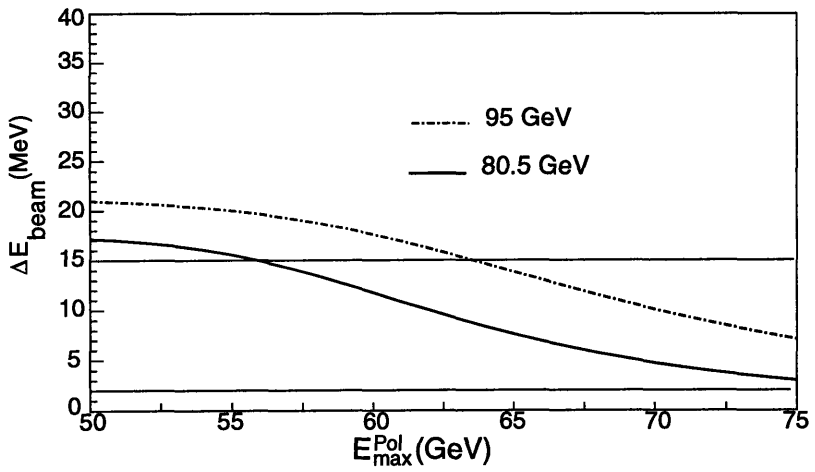

Figure 6: Predicted beam energy resolution as a function of maximum energy at which polarization is possible $E^{\rm pol}_{\rm max}$, for $E_{\rm beam}$ = 80.5 and 95 GeV [39]. The line at 2 MeV represents the LEPI resolution.

lead-scintillator ring calorimeter at low polar angles[2], a scintillation counter system, a uranium hadron calorimeter with proportional wire chamber readout, and an accurate muon chamber system, including the recently added Forward Backward Muon Chambers [46] which extend the polar angle range down to 24°. These detectors are installed in a 12 m diameter magnet which provides a solenoidal field of 0.5 T and a toroidal field of 1.2 T. The luminosity is measured using BGO calorimeters [47] situated on each side of the detector. A perspective view is shown in figure 7.

The task of the detector is to record the final state, which consists of electrons, photons, muons, "jets" of charged and neutral hadrons from quark hadronization or hadronic tau decay, and neutrinos, which are not detected, but identified as missing energy and momentum. Different combinations of subdetectors are used to measure the energy and momentum of these particles, thus detector description is logically done in terms of sensitivity to different pieces of the final state.

Electrons are identified by a track from the central tracking system pointing at a large local energy deposition in the BGO (a "bump") which is consistent in shape with an electromagnetic shower. The track is required to distinguish electrons from photons, which otherwise have an identical signature. Thus, electron identification is

[2]In the right-handed L3 coordinate system, the z axis is parallel to the e^- direction, and the x axis points to the center of the LEP ring.

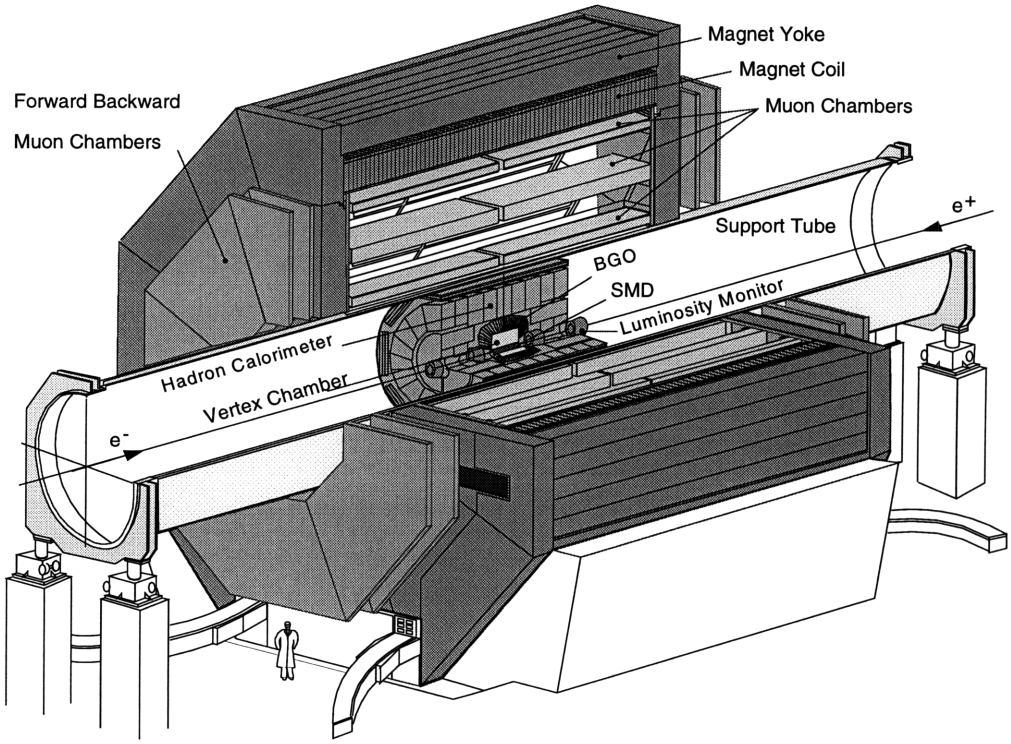

Figure 7: Perspective view of the L3 detector.

a process of matching tracks to bumps, and the acceptance is limited by the geometry of the central tracker. Energies and angles of electrons and photons are measured in the BGO, which has roughly 1% energy resolution and 10 mrad angular resolution. The BGO covers 92% of the solid angle, with gaps for the beampipe and the seam between the barrel and endcap sections.

Muons are detected in the muon drift chamber system, which has 2.5% energy resolution, and 10 mrad angular resolution. The muon chamber system, accounting for deactivated cells, covers roughly 80% of the solid angle, and the gaps can be covered by using the muon minimum ionizing signature, consisting of a track in the central tracking chamber pointing at small energy depositions in the BGO and hadronic calorimeters. Using this signature to identify muons increases overall muon detection efficiency, but with degraded energy and angular resolutions.

Jets are detected by multiple nearly collinear tracks pointing to energy depositions ("clusters") in both the BGO and Hadron calorimeters. Energy and angular resolutions on jets are given by a combination of track and calorimeter information

which depends on geometry and method of combining tracks and depositions into jets ("jet clustering"). Typical jet energy resolution is 20% and angular resolution 40 mrad, where the resolution is taken from the difference between the jet and the original quark. The calorimeter system covers around 98% of the solid angle.

The assembly of the data signals into an event takes place in two steps. First, the raw data from each subdetector is converted to an energy or position measurement using calibration parameters specific to the subdetector. Each subdetector is calibrated using both an independent calibration system, typically measuring the response from a known input, and also from $e^+e^- \to Z \to f\bar{f}$ data at $\sqrt{s} = M_Z$ where the fermion energies and momenta are known from four momentum conservation. Subsequently, the tracks, bumps, and clusters are assembled from these measurements, and linked accross subdetectors, forming the signatures of the particles composing the event.

Computer simulation of the physical processes is a necessary component of the construction of an analysis, as the means to understand selection efficiencies and sample purities, control systematic errors, and understand the detector response to the particles passing through it. Because analytical formulae are not available to describe these processes, random sampling ("Monte Carlo") techniques are used [48]. Event generators simulate events (KORALW [49] or EXCALIBUR [50] for four fermion events, PYTHIA [51] for all other processes) which are then passed through a model for detector response. The response of the L3 detector is modelled with the GEANT [52] detector simulation program which includes the effects of energy loss, multiple scattering and showering in the detector materials and in the beam pipe. This process provides high statistics simulated event samples which are used to build physics analyses for use on data.

3.3 Data Samples

In the summer of 1996, the L3 detector recorded a total integrated luminosity of 11 pb^{-1} at $\sqrt{s} = 161.34 \pm 0.06$ GeV. This center of mass energy coincides with the kinematic threshold of the process $e^+e^- \to WW$, and will be called the "threshold sample". After the installation of more accelerating cavities, the center of mass

energy was increased, and the L3 detector recorded a total integrated luminosity of 1.00 pb^{-1} at 170.31 ± 0.06 GeV and 9.25 pb^{-1} at 172.32 ± 0.06 GeV. For the results presented in this thesis these two data samples are combined for a total of 10.25 pb^{-1} at a luminosity weighted center of mass energy of 172.13 ± 0.06 GeV, and will be called the "high energy sample". For both data sets, the luminosity was measured with an accuracy of 0.6% [53] and the beam energy was measured with an accuracy of 30 MeV [54].

4 Selection of W-pair events

The first step in any analysis of W-pair physics is the distillation of the W-pair events from the full data sample, by applying a selection algorithm with high efficiency for the signal and low efficiency for everything else, ensuring a pure sample. Thus the following selections are determined from Monte Carlo studies balancing these two criteria.

The four fermion final states from the decay of a pair of W bosons are conveniently grouped into three semileptonic final states ($qqe\nu$,$qq\mu\nu$,$qq\tau\nu$) each with branching fraction $\sim$ 15%, one fully leptonic final state ($\ell\nu\ell\nu$) with branching fraction $\sim$ 11%, and one fully hadronic final state ($qqqq$) with branching fraction $\sim$ 45%. For all modes of decay, each fermion has $\sim \sqrt{s}/4 \sim$ 40 GeV of energy and is difficult to miss provided it is within the fiducial volume of the detector. Selection algorithms for each final state use criteria based on the kinematics of the final state particles to distinguish the signal from the backgrounds, as summarized below. Further details on the selection criteria can be found in references [55] and [56].

It is beneficial to consider the background conditions before discussing selection algorithms for the specific final states. The are essentially three sources of high energy fermions producing background for W-pair events; difermion production ($e^+e^- \rightarrow Z/\gamma \rightarrow f\bar{f}$), singly resonant W production ($e^+e^- \rightarrow We\nu$; for example, diagram b of figure 3), and multiple boson production (mostly $e^+e^- \rightarrow ZZ \rightarrow f_1\bar{f}_1f_2\bar{f}_2$). For the energies of LEPII, the expected cross sections from different sources are shown in figure 8.

The background from difermion production dominates the W-pair signal by two orders of magnitude at 161 GeV, falling to one order of magnitude at 172 GeV, mostly due to the rapid increase in the signal cross section. This background can only produce either 40 GeV quarks or 40 GeV leptons of the same family, thus is easily seperated from final states with both high energy quarks and leptons ($qq\ell\nu$) or high energy leptons of different families ($\ell_1\nu_1\ell_2\nu_2, \ell_1 \neq \ell_2$). Furthermore, a significant portion of this background comes from "radiative return" events, where one incoming particle

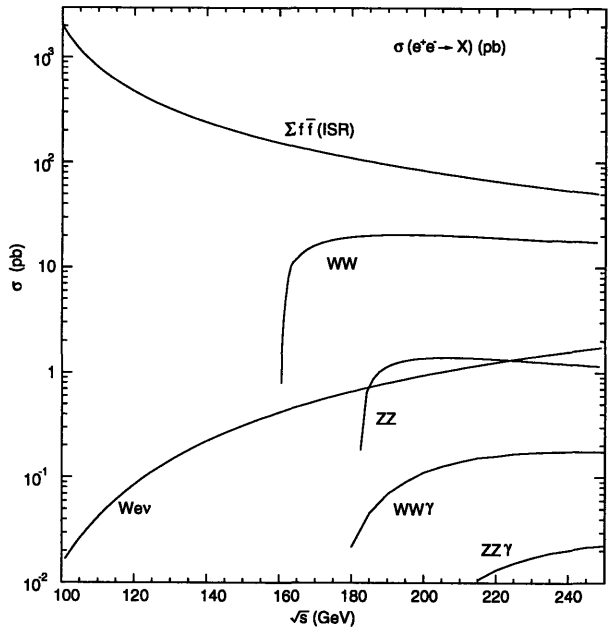

Figure 8: Cross sections for $e^+e^- \to X$ vs $\sqrt{s}$. Two fermion background clearly dominates W-pair production [57]. Also shown is single W production $e^+e^- \to We\nu$ (e.g. diagram b of figure 3) and other multiple boson production cross sections.

radiates a photon, thus changing the effective center of mass energy to $\sqrt{s} \sim M_Z$ (Fig. 9). The photon polar angle distribution is sharply forward peaked, meaning the photon travels down the beampipe undetected, resulting in reduced visible energy and longitudinal energy imbalance. These characteristics can be used to remove much of this background from the data sample (Fig. 10).

In contrast, the cross sections for single W production and multiple boson production are smaller than the signal cross section (Fig. 8). In single W production, the electron is produced at very low polar angles, thus escaping detection and leaving only the decay products of one W in the detector, which allows the seperation of this background from the signal. Of the multiple boson processes, only $e^+e^- \to ZZ \to f_1\bar{f}_1 f_2\bar{f}_2$ has a sufficiently large cross section to be considered as potential background. Only the fully hadronic final state and the fully leptonic final state where both bosons decay to the same lepton family ($e^+e^- \to WW/ZZ \to \ell^+\nu\ell^-\bar{\nu}/\ell^+\ell^-\nu\bar{\nu}$) of the signal and this background can have identical leptonic content. For the fully hadronic state, the signal and background signatures are nearly identical, and the small background

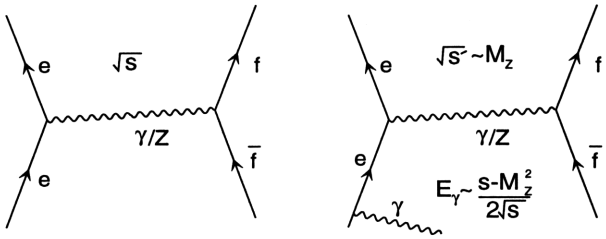

Figure 9: Feynman diagrams for fermion pair production without and with initial state radiation. The energy of the radiated photon is typically 54 (62) GeV for the threshold (high energy) sample.

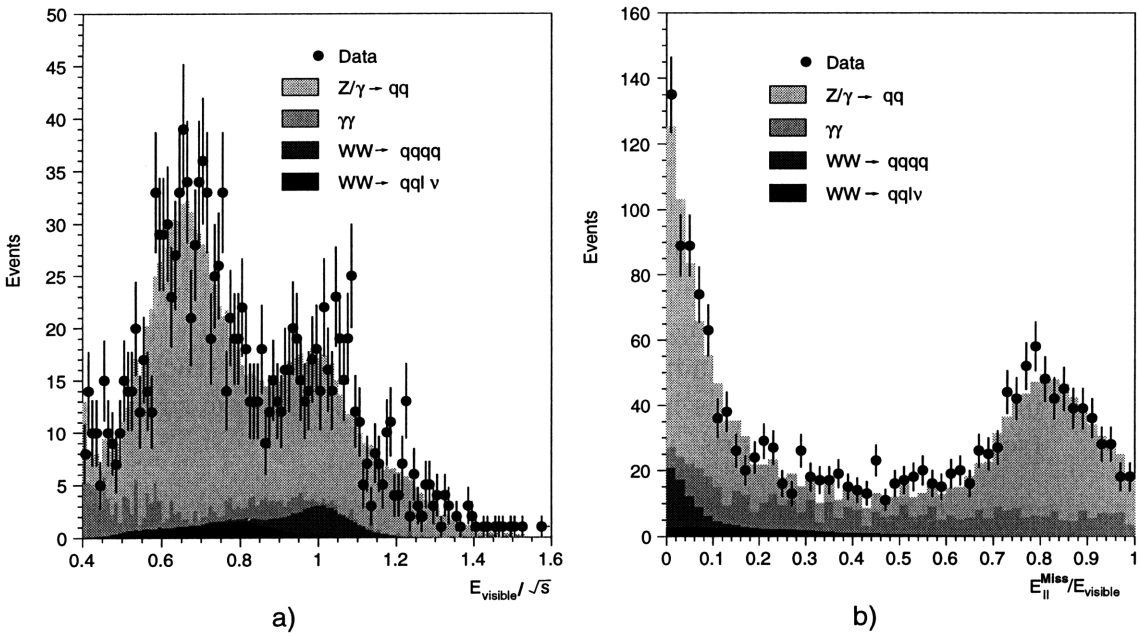

Figure 10: Distributions of a) visible energy and b) longitudinal energy imbalance, for data at the preselection level, with Monte Carlo expectations. The "radiative return" events are observed as the large peaks at low visible energy and high longitudinal energy imbalance.

is essentially irreducible, while for the fully leptonic final states, differences in the lepton opening angles can be used to distinguish signal from background.

4.1 Selection of $qqe\nu$ final states

The selection of events where one W decays hadronically and the other to an electron and its associated neutrino requires a spatially isolated high energy electron in the detector, hadronic activity, and high missing energy since the neutrino escapes undetected. These criteria, with requirements of high invariant masses of the lepton-

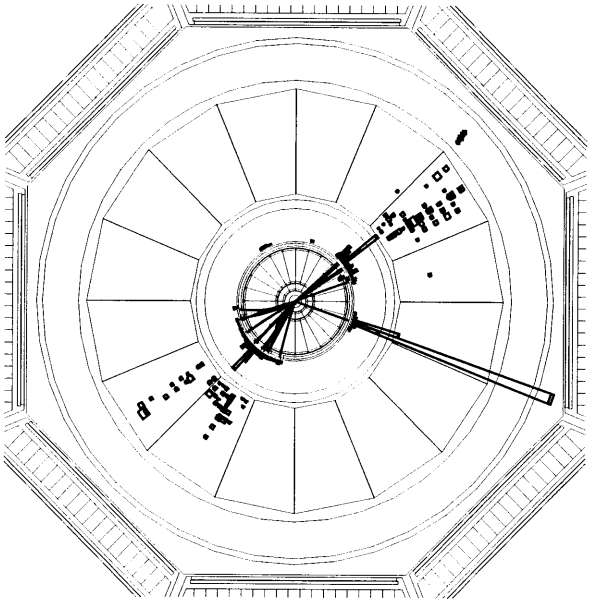

Figure 11: A $qqe\nu$ candidate event from the data, in the plane transverse to the beampipe ($r\phi$ plane). From the interaction point (center), there is one isolated track pointing at a 37 GeV BGO bump (tower to the right) forming the electron candidate, and two sets of multiple tracks pointing at energy depositions in the BGO (towers) and hadronic calorimeter (squares), which comprise the hadronic system.

neutrino and jet-jet systems, and appropriate fiducial volume cuts on the missing energy to distinguish the neutrino from a "radiative return" photon in the beam pipe all but eliminate the backgrounds from the sample. The final selection is 76% (79%) efficient for signal for threshold (high energy) samples, with better than 95% purity for both. The loss in efficiency is dominated by the geometrical acceptance limits of the L3 detector at low polar angles. A candidate $qqe\nu$ event is shown in figure 11.

4.2 Selection of $qq\mu\nu$ final states

The selection of events where one W decays hadronically and the other to a muon and its associated neutrino requires a spatially isolated high energy muon in the detector, hadronic activity, and large missing energy since the neutrino goes undetected. At 161 GeV, only the muon chamber system is used to identify the muon, while at 172 GeV, the muon identification is an OR between a selection using the muon chambers and one using the minimum ionizing signature in the calorimeters, for muons which

slip through a gap in the muon chambers. Again, additional requirements of high invariant masses of the lepton-neutrino and jet-jet systems and appropriate fiducial volume cuts are applied, producing a selection with 66% (79%) efficiency for the threshold (high energy) sample and better than 95% purity for both samples.

4.3 Selection of $qq\tau\nu$ final states

Unlike the lepton of the previous final states, the tau decays near ($\sim$ 1 mm) the interaction point, 35% of the time to a tau neutrino and electron-neutrino or muon-neutrino pair, 65% to a tau neutrino and hadrons, which makes this final state more difficult to select. Along with two hadronic jets and missing energy from the neutrinos, the event has either an isolated lepton or a jet from the decay of the tau. In the former case, the selection is a variation of the other semileptonic selections, and has similar efficiency. For the hadronic tau decays, the tau jet identification is the crucial element. The selection looks for a three jet system where the tau jet is of lower energy, has smaller track multiplicity, and is more collimated, compared with a typical hadronic jet. The resulting efficiency is $\sim$ 50%, due to the necessary supression of large background from diquark events with a radiated gluon (Fig. 13), which is very similar in appearance. The resulting overall selection efficiency for this channel is 37% (47%) for purities of 57% (80%) for the threshold (high energy) sample. A candidate $qq\tau\nu$ with hadronic tau decay is shown in figure 12.

4.4 Selection of $\ell\nu\ell\nu$ final states

The final states where both Ws decay leptonically have the characteristics of considerable missing energy from the neutrinos and two energetic well seperated leptons or a lepton and a tau jet, thus the selections are the appropriate adaptation of the semileptonic selections. Background from dilepton final states is characterized either by two back to back leptons, or with initial state radiation, a planar event where the plane is defined by the directions of one lepton and the initial state photon, taken to be the beam axis. This background is removed by requiring one lepton to lie out of

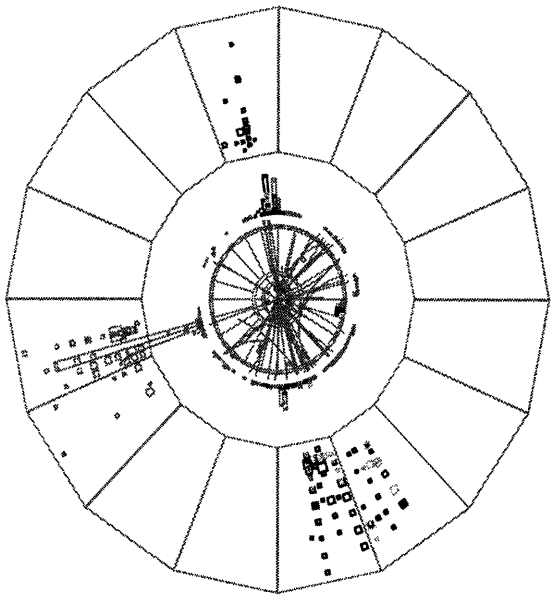

Figure 12: A $qq\tau\nu$ candidate event from the data. The tau candidate is the left-most jet.

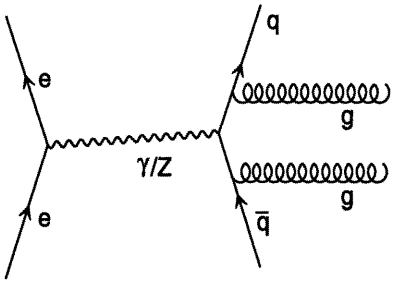

Figure 13: Feynman diagram for the dominant background $qqg(g)$ for the $qq\tau\nu$ channel (one gluon) when the tau decays hadronically and the $qqqq$ channel (two gluons).

the plane defined by the other lepton and the beam axis. Selections based on these criteria have efficiencies of 40% (45%) for purities of 80% (95%) for the threshold (high energy) data. These efficiencies are consistent with simple calculations using the semileptonic selection efficiencies and the expected branching ratios. A candidate $e\nu\mu\nu$ event is shown in figure 14.

4.5 Selection of $qqqq$ final states

The selections for final states with leptons are built around the signature of at least one highly energetic visible lepton and missing energy from at least one energetic

neutrino, which effectively seperates the signal from the background for both data samples. For the fully hadronic ("four jet") final state, there is no such distinctive signature to seperate signal from background, thus the selection is more difficult. In particular, diquark production with strong interactions in the final state producing four jets ($e^+e^- \rightarrow Z/\gamma \rightarrow$ *qqgg*, Fig. 13) constitutes a large irreducible background. The high background conditions at threshold necessitate the use of a neural network for seperation, while at higher energies the increase in the signal cross section allows the use of a straightforward cut based analysis.

In both types of analysis, the events are first passed through a preselection to sift candidate events from the full data sample. The preselection uses loose requirements on visible energy, energy balance, and event topology to retain the signal events but remove unwanted events, mostly from two-photon events ($e^+e^- \rightarrow e^+e^-+$ hadrons), cosmic rays, and machine related background. At threshold, the preselection is more stringent, retaining 88% of the W-pair events. At higher energy, the preselection can be relaxed, retaining more than 99% of the signal. After preselection, the tracks and calorimetric depositions are clustered into 4 jets using the Durham [58] algorithm for the final selection.

The algorithms for final seperation of signal and background for both data samples use essentially the same criteria. Fully hadronic events do not have highly energetic photons or leptons, so criteria based on missing energy, momentum imbalance, and visible lepton and photon energy seperate signal events from "radiative return" events and W-pair semileptonic events. Subsequently, differences in the multiplicity, event topology, and kinematics are exploited to distinguish W-pair hadronic events from the remaining background. Jets from quarks on average contain more charged particles than jets from gluons, so requirements on jet charged multiplicity helps seperate signal from background. Furthermore, the different processes will produce different event shapes, since gluon radiation tends to produce jets nearly collinear with the initial quark, while in W-pair events the jets are more seperated, making W-pair events more isotropic. Finally, the fact that W-pair jets come from Ws is reflected in the kinematics of the jets, so jet energies and invariant masses of jet pairs can be used to

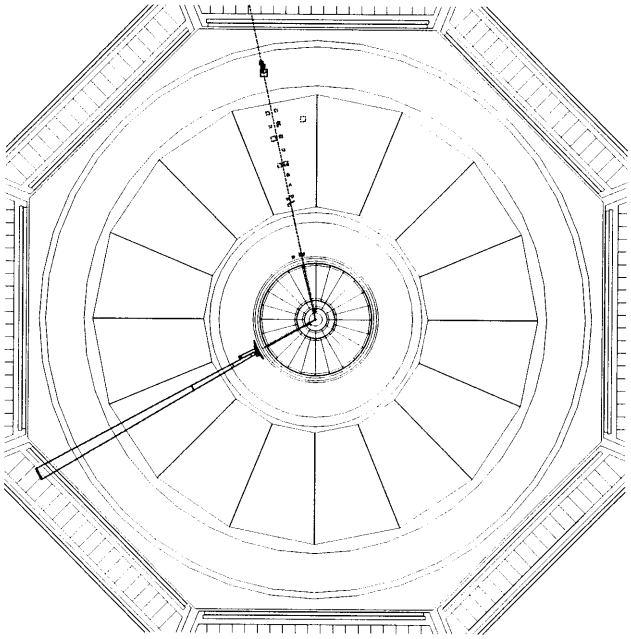

Figure 14: A $e\nu\mu\nu$ candidate event from the data. The muon (track heading up) leaves its minimum ionizing signature in the calorimeters and is measured in the muon chambers (outside the picture).

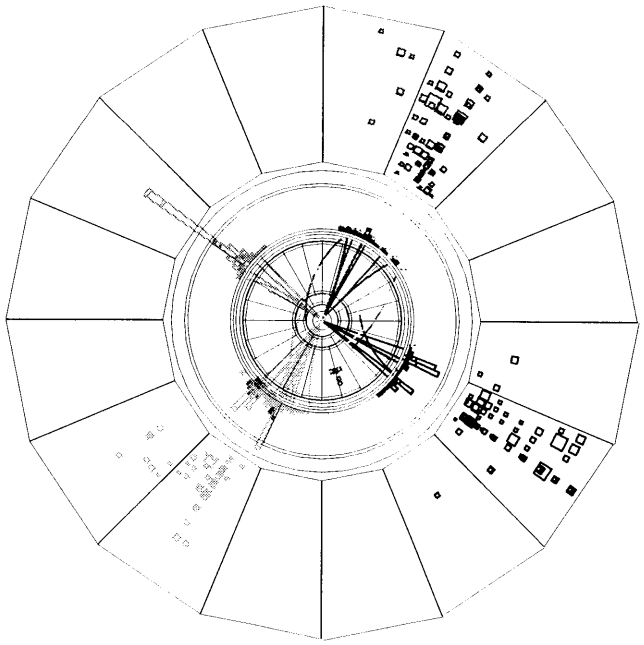

Figure 15: A $qqqq$ candidate event from the data, in the $r\phi$ plane.

distinguish signal from background. A candidate $qqqq$ event is shown in figure 15.

For the threshold data, a feed-forward neural network [59] is used to take advantage of the correlations between selection variables for optimum seperation, thereby incorporating the major background instead of rejecting it. After preselection and clustering, all events are fed into the neural network, which uses 12 different input observables sensitive to four jet topology, signal kinematics, and background kinematics as described above. The neural network is trained on simulated events such that the output for signal peaks at 1 and for background at 0. The resulting output distribution for data is fit to a linear combination of the distribution shapes from simulated pure signal and pure background with the normalizations left free to derive cross sections for both signal and background.

At higher center of mass energies, the background drops off mildly and the signal increases, such that imposing simple requirements on the minimum set of discriminating variables seperates signal from background, avoiding the complexities of correlating all the selection variables via a neural network. Using visible energy, leptonic energy, energy imbalance, jet multiplicity and event shape lead to a selection with 79% efficiency for a purity of 80%.

4.6 Cross Efficiencies and Systematic Errors

Cross efficiencies

While each selection is designed to select only its own decay mode, there is some residual efficiency for the other W-pair decay modes, which can be treated as signal instead of background, therefore reducing the background cross sections. This "cross efficiency" between decay channels is greatest for $qq\tau\nu$ and $qqe\nu$ or $qq\mu\nu$, where leptonic decays of the tau are selected by the other selections, and vise versa. To account for this, instead of a number for the signal efficiency, a matrix is used, with off-diagonal entries of order 5% for the semileptonic selections, which reduces the corresponding background cross sections by up to 50%. The selection efficiency matrix and accepted background cross sections are listed in table 3.

Selection Channel	Efficiency [%] for $e^+e^- \to WW \to$ $qqqq$	$qqe\nu$	$qq\mu\nu$	$qq\tau\nu$	$\ell\nu\ell\nu$	Background [pb]
Threshold Data						
$qqe\nu$	—	60.1	—	1.40	—	0.016
$qq\mu\nu$	—	—	66.0	2.10	—	0.016
$qq\tau\nu$	0.10	4.70	4.80	37.5	—	0.157
$\ell\nu\ell\nu$	—	—	—	—	43.3	0.040
High Energy Data						
$qqqq$	78.85	0.36	0.42	2.93	—	1.31
$qqe\nu$	—	73.4	0.15	1.80	—	0.073
$qq\mu\nu$	—	0.09	78.7	1.99	—	0.035
$qq\tau\nu$	0.54	5.23	7.03	45.6	—	0.254
$\ell\nu\ell\nu$	—	—	—	—	43.7	0.019

Table 3: Selection efficiency matrices and accepted background cross sections from non W-pair processes at 161 and 172 GeV.

Systematic errors

All selections are based on Monte Carlo simulation, thus the main source of systematic error is discrepency between the simulation and data. These errors are estimated by comparison of selection variable distributions from simulation to the same from data, both on the W-pair samples and simulation and data from LEPI, where the data samples are much larger, so deviations can be distinguished from statistical effects. In addition, theoretical dependencies on simulation input parameters and different event generation models are assessed by variation of the input parameters and event generators. Finally, effects from mismeasurement of the fermion energies and angles are estimated by artificial perturbation of the energy and angular measurements of simulated events, using the detector resolutions. The result of such studies is the estimation of systematic errors on signal and background efficiencies, which are propagated to analyses using these particular selections. Typically the systematic errors on signal efficiencies are $\sim$ 5%, and on background efficiencies between 5 and 20% (all relative), depending on selection channel. In all cases, the resulting systematic error is smaller than the statistical error.

5 Measurement of Cross Sections and Branching Ratios

The first and most obvious measurements to make after selecting the W-pair events are the production cross section and branching ratios measurements. After applying necessary corrections, the cross section/branching ratios measurements are a simple application of Poisson statistics implemented in a fit.

5.1 Non W-pair Interference

There are additional contributions to the four fermion final state cross section arising from processes not involving the production of a pair of W bosons, as explained in section 2.1 (Fig. 3), which lead to corrections to obtain the W-pair cross sections. For high invariant masses of resulting fermion pairs and fermions within the acceptance of the detector, at the current level of statistical accuracy these corrections are non-negligible only for the $qqe\nu$ and $\ell\nu\ell\nu$ channels. The efficiencies for these channels include multiplicative correction factors of 1.27 and 0.92 (1.10 and 1.03) respectively for the threshold (high energy) data samples to extract the W-pair contribution from the measured cross section. The correction factors are determined from Monte Carlo studies including and neglecting the extra diagrams, and the correction error of order 1% is included in the systematic errors.

5.2 Cross section and branching ratios determinations

In general, the measured cross section σ follows from the number of events selected N, for a given efficiency ϵ, luminosity, $\mathcal{L}$, and background cross section σ^{bg}:

$$\sigma = \frac{N}{\mathcal{L}\epsilon} - \sigma^{\mathrm{bg}}$$

However, in order to take advantage of the cross efficiencies, the cross sections, σ_i, of the signal processes ($i = qqqq, qqe\nu, qq\mu\nu, qq\tau\nu, \ell\nu\ell\nu$) are determined simultaneously

Process	$\mathcal{L}$ [pb^{-1}]	N_{data}	σ_i [pb]	σ_{SM} [pb]
Threshold Sample				
$qqqq$	10.3	–	$0.98^{+0.50}_{-0.40} \pm 0.05$	1.76
$qqe\nu$	10.3	4	$0.62^{+0.38}_{-0.28} \pm 0.02$	0.56
$qq\mu\nu$	10.9	4	$0.53^{+0.33}_{-0.24} \pm 0.01$	0.56
$qq\tau\nu$	10.3	3	$0.22^{+0.55}_{-0.38} \pm 0.08$	0.56
$\ell\nu\ell\nu$	9.6	2	$0.39^{+0.43}_{-0.27} \pm 0.02$	0.41
High Energy Sample				
$qqqq$	10.25	57	$5.33^{+0.97}_{-0.89} \pm 0.14$	5.66
$qqe\nu$	10.25	19	$2.44^{+0.64}_{-0.55} \pm 0.04$	1.81
$qq\mu\nu$	10.25	9	$1.06^{+0.44}_{-0.36} \pm 0.03$	1.81
$qq\tau\nu$	10.25	12	$1.60^{+0.80}_{-0.67} \pm 0.06$	1.81
$\ell\nu\ell\nu$	9.76	9	$1.93^{+0.74}_{-0.60} \pm 0.05$	1.32

Table 4: Total luminosity used, $\mathcal{L}$, number of selected data events, N_{data}, and resulting individual cross sections. The first error is statistical and the second systematic. Also shown are the Standard Model expectations for a W mass of 80.356 GeV [20].

in one maximum likelihood fit. The total likelihood L is given by the product of Poisson probabilities P for channel i to select N_i events given an expected μ_i events:

$$\begin{aligned} L &= \prod_i P(N_i, \mu_i) \\ \mu_i &\equiv \mathcal{L}_i \cdot \left(\sum_j \epsilon_{ij}\sigma_j + \sigma_i^{\text{bg}} \right) \end{aligned}$$

where $\mathcal{L}_i, \sigma_i$ and σ_i^{bg} are the luminosity and signal and background cross sections for channel i and ϵ_{ij} is the efficiency matrix of section 4.6. The luminosity and number of events are measured, the efficiencies and background cross sections taken from simulation, and the signal cross sections are the fit parameters. For the $qqqq$ channel at threshold, the Poisson probability is replaced by the cross section dependent likelihood function derived from the neural network fit described in section 4.5. The efficiency matrix and background cross sections are given in table 3, and the results for the individual channels are given in table 4.

The same formalism is used to determine the total cross section σ_{WW} and branch-

Parameter	Lepton Non-Universality	Lepton Universality	Standard Model
$B(\mathrm{W} \to \mathrm{e}\nu)$ [%]	$16.8^{+3.7}_{-3.3} \pm 0.3$	—	
$B(\mathrm{W} \to \mu\nu)$ [%]	$8.5^{+2.9}_{-2.4} \pm 0.2$	—	
$B(\mathrm{W} \to \tau\nu)$ [%]	$11.0^{+4.2}_{-3.9} \pm 0.4$	—	
$B(\mathrm{W} \to \ell\nu)$ [%]	—	$12.1^{+1.3}_{-1.3} \pm 0.2$	10.8
$B(\mathrm{W} \to qq)$ [%]	$63.6^{+3.9}_{-4.0} \pm 0.5$	$63.6^{+3.8}_{-4.0} \pm 0.4$	67.5
σ_{WW} [pb] 161 GeV	$2.90^{+0.82}_{-0.71} \pm 0.07$	$2.91^{+0.81}_{-0.70} \pm 0.07$	3.87
σ_{WW} [pb] 172 GeV	$12.17^{+1.49}_{-1.39} \pm 0.17$	$12.20^{+1.46}_{-1.36} \pm 0.18$	12.41
Using Standard Model Branching Ratios			
σ_{WW} [pb] 161 GeV	$2.87^{+0.80}_{-0.69} \pm 0.08$		3.87
σ_{WW} [pb] 172 GeV	$12.13^{+1.43}_{-1.34} \pm 0.18$		12.41

Table 5: W branching ratios and total W-pair cross sections with and without the assumption of lepton universality, and cross sections imposing Standard Model branching ratios. The first error is statistical and the second systematic. Also shown are the Standard Model expectations.

ing ratios $B(\mathrm{W} \to ff')$ with the simple substitution:

$$\begin{aligned} \sigma_i &= r_i \cdot \sigma_{\mathrm{WW}} \\ \text{with } & r_{qqqq} = (B(\mathrm{W} \to qq))^2 \\ & r_{qq\ell\nu} = 2 \times (B(\mathrm{W} \to qq)(B(\mathrm{W} \to \ell\nu) \\ & r_{\ell\nu\ell\nu} = (1 - B(\mathrm{W} \to qq))^2 \end{aligned}$$

where the sum of all branching ratios is constrained to unity. The branching ratios are either fit parameters with or without the assumption of lepton universality, or are fixed to the Standard Model values for a more accurate determination of σ_{WW}. The branching ratios are independent of energy, thus the two data sets are combined to improve the branching ratio measurement. The results for the branching ratios and total cross sections are listed in table 5.

Systematic errors

The estimation of the cross section and branching ratios systematic errors follows directly from the systematic errors from selections, propagated through the fit. The efficiency matrix, the luminosity, and the background cross sections are all varied by their respective systematic errors to derive a systematic error on the measured cross sections and branching ratios. For the $qqe\nu$ and $\ell\nu\ell\nu$ final states, the higher order correction error of 1% is included as an systematic error on the efficiency. The results are shown in tables 4 and 5. Cross checks using similar selection algorithms produce consistent results. In addition, the two methods of signal seperation for the $qqqq$ final state also yield consistent results. In all cases, the systematic error is small in comparison with the statistical error.

5.3 Results

The results in tables 4 and 5 are dominated by the statistics of small samples. The statistical errors correspond to 68% confidence levels, derived by varying the fit parameter to produce a change of 0.5 in the logarithm of the likelihood. With this in mind, no significant deviations from the expectations are seen. This observation is illustrated by figure 16, which shows the total cross sections compared to theory. The high energy data point favors the existence of the trilinear gauge boson couplings by rougly 2σ. This is confirmed by a dedicated measurement of the couplings using the same data sets, which exclude a vanishing ZWW coupling at more than 95% confidence level [60]. The branching ratios results are consistent with the assumption of lepton universality.

Using the hadronic branching ratio of $63.6^{+3.8}_{-4.0}\pm0.4$ with the other 5 CKM elements involved from the particle data book without unitarity constraints [29], and the strong coupling constant $\alpha_s(\sqrt{s} = \mathrm{M_W}) = 0.123$ [26], the equation of section 2.2 gives:

$$|V_{cs}| \;=\; 0.80^{+0.18}_{-0.18} \pm 0.02$$

The error includes the error from the other matrix elements and α_s but is dominated

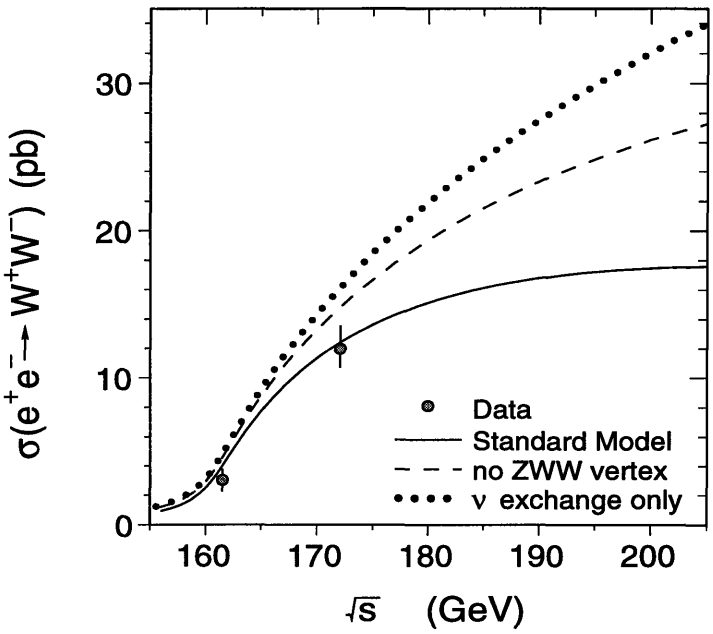

Figure 16: Measured W-pair cross sections, using Standard Model branching ratios, compared with theory with different combinations of couplings.

by the statistical error on the branching ratio measurement. This result is consistent with the current world average [29].

6 Measurement of W Mass

The measurement of the W mass uses different methods appropriate to the different energies. At threshold, the dependence of σ_{WW} on M_W given by the Standard Model is exploited, while at 172 GeV, M_W is determined using the invariant mass spectrum reconstructed from the decay products.

6.1 Threshold method

The "threshold method" [33] is essentially a reinterpretation of the cross section measurement in terms of mass, using the mass dependence predicted by the Standard Model. All other parameters, including the W width and trilinear gauge couplings, are set to the Standard Model values. The dominant source of the mass dependence is the integration over the Breit-Wigner densities of the W bosons:

$$\begin{aligned} \sigma_i &= r_i^{SM} \cdot \sigma_{WW}(\sqrt{s}, M_W) \\ \sigma_{WW}(\sqrt{s}, M_W) &= \int_0^s ds^+ \rho(s^+) \int_0^{(\sqrt{s}-\sqrt{s^+})^2} ds^- \rho(s^-) \sigma(s, s^+, s^-) \\ \rho(m^2) &= \frac{1}{\pi} \frac{m\Gamma_W}{|m^2 - M_W^2 + im^2\Gamma_W/M_W|^2} \end{aligned}$$

where $\rho(m^2)$ is the Breit-Wigner density for a W boson with mass M_W, width Γ_W, and invariant mass m. The evaluation of these integrals and rest of the rather involved calculation of $\sigma(s, s^+, s^-)$ are determined using the semi-analytical integration program GENTLE [61], which accounts for initial state radiation and radiative corrections, and is not very transparent.

The cross section dependence on mass varies with center of mass energy $\sqrt{s}$, being most sensitive just above threshold, which motivates the collection of the threshold sample. This is due to the abrupt rise in the cross section just after the kinematic threshold, which is set by the W mass. Detailed studies [33] of the optimum $\sqrt{s}$ which minimizes statistical error on M_W confirm this assertion (Fig. 17).

The experimental determination of M_W is simply the cross section fit of section 5.2 repeated, with M_W replacing σ_{WW} as the only free parameter. The essence of

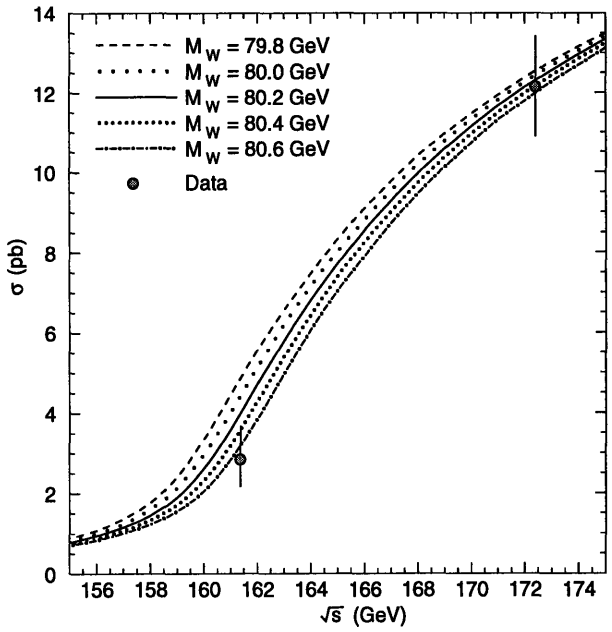

Figure 17: Total W-pair cross section vs $\sqrt{s}$ for various values of M_W.

the fit is illustrated in figure 18, which uses only the threshold sample, giving:

$$M_W = 80.82^{+0.47}_{-0.40}\ \text{GeV}$$

Using both the threshold and high energy samples improves the result only slightly

$$M_W = 80.84^{+0.44}_{-0.40}\ \text{GeV}$$

despite the large increase in number of events, confirming the importance of the choice of center of mass energy.

Systematic errors

Systematic errors for the threshold method mass determination come from errors in the center of mass energy, the event selection, and the mass dependence calculation. At threshold, the cross section is essentially a function of a single variable $x = \sqrt{s} - 2M_W$, which implies the error of 30 MeV [54] on the beam energy translates directly into an error on M_W. The systematic error from event selection is calculated in the same way as in section 5.2, by varying the fixed parameters of the fit by their errors,

and assessing the effect on the fit result, which results in a 50 MeV error.

The two sources of theoretical error from GENTLE reflect the uncertainties in the input to the program and the accuracy of the calculation itself. The dominant input uncertainty is the W width $\Delta\Gamma_W$, which contributes $\sim \Delta\Gamma_W/6$ to the uncertainty in M_W [33]. Using the current world average of $\Delta\Gamma_W = 0.06$ GeV [62] leads to a 10 MeV systematic error on the W Mass. The accuracy of the calculation itself is assessed by tests against other calculations [63]. The resulting calculation error is of order 10^{-3} pb, translating into an error of ~ 1 MeV on M_W. Thus, the final W Mass from the threshold method at 161 and 172 GeV is

$$M_W = 80.84^{+0.44}_{-0.40} \pm 0.03 \text{ (LEP)} \pm 0.05 \text{ GeV}$$

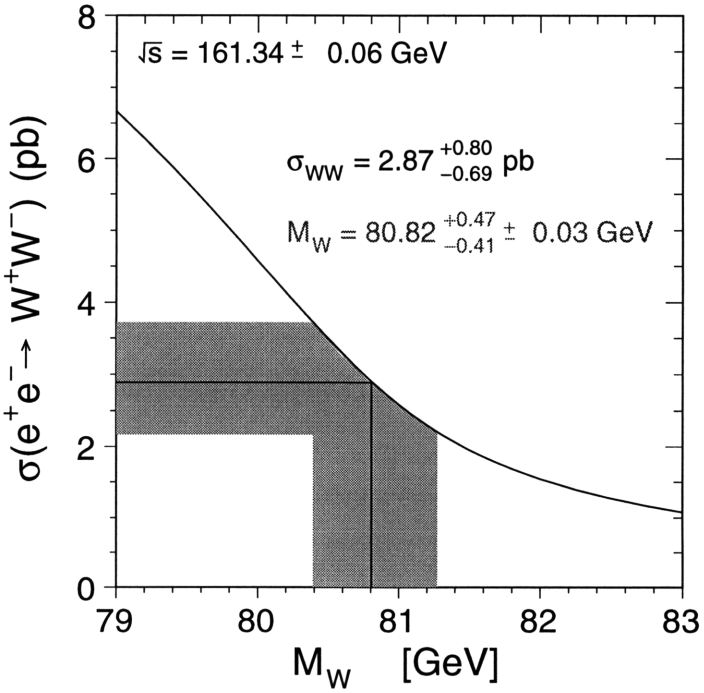

Figure 18: Total W-pair cross section as a function of M_W at $\sqrt{s} = 161.34$ GeV. The curve is the Standard Model expectation, the horizontal band the cross section measurement, and the vertical band the resulting measurement of M_W.

6.2 Direct Reconstruction

At and above $\sqrt{s} = 172$ GeV the W-pair production cross section is large enough to provide sufficient statistics for the use of the "direct reconstruction method" [33], which entails constructing the invariant mass spectrum directly from the four momenta of the W decay products and fitting for the W mass. The data sample for the 172 GeV data consists of 57 $qqqq$ events, 19 $qqe\nu$ events, 9 $qq\mu\nu$ events, and 12 $qq\tau\nu$ events, selected as in section 4. The $\ell\nu\ell\nu$ channel cannot be used in direct reconstruction, due to the lack of mass information.

A simple estimate for the statistical error on the W mass ΔM_W^{stat} given the width Γ_W, the invariant mass resolution σ_m, and the number of events N in the distribution

$$\Delta M_W^{stat} \approx \sqrt{\frac{\Gamma_W^2 + \sigma_m^2}{N}}$$

shows that the improvement in σ_m translates directly into a smaller statistical error on the W mass. The invariant mass resolution is improved significantly by the use of a kinematic fit incorporating four momentum conservation. The kinematic fit allows the energies and angles of the reconstructed fermions to vary within the detector resolutions to satisfy the constraints imposed, by an application of the method of Lagrange multipliers [33]. An additional constraint of equal masses of the W bosons within the W width further improves resolution. Resolutions in average invariant mass typically improve by a factor of 3 after the kinematic fit, as shown in figure 19. For the $qq\tau\nu$ channel, there are not enough constraints to perform the fit, so instead energy conservation is imposed by rescaling the jet energies such that the sum equals $\sqrt{s}/2$. This results in improved resolution on the hadronic system invariant mass, which is used to create the spectrum.

For the fully hadronic channel, there is no flavor or charge identification of the jets, so there is no way to know which jets come from which W. This results in a threefold ambiguity in how to pair up the four jets into two Ws for the kinematic fit. Monte Carlo studies show that choosing the pairing combination with the maximum of the smallest of the two jet-pair opening angles selects the correct pairing in 79%

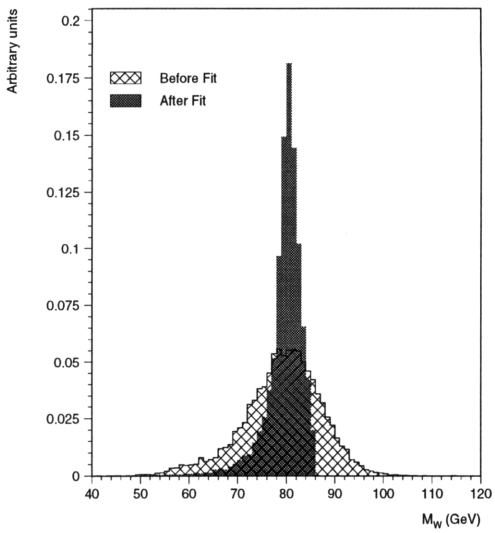

Figure 19: Effect of the kinematic fit on average invariant mass, for $qqqq$ events at $\sqrt{s} = 172$ GeV. The resolution improvement is a factor of 3.

of the cases, compared to 33% from arbitrary guessing. This is due to the fact that at 172 GeV the Ws have velocity $\beta \sim 0.36$, so for the correct pairing the typical opening angle for both pairs is $\sim 140°$. For mismatched pairs, naively assuming a flat distribution for the opening angle, the probability that the opening angle will be less than 140° is $\frac{140}{180} = 0.77$ which agrees well with the Monte Carlo studies. The expected mismatched event contribution is treated as an extra background when fitting the data spectrum.

Of the several ways to extract the mass from the invariant mass spectrum the conceptually easiest is the "Monte Carlo Calibration" method [33]. This entails calibration of an analytical function with an estimator for the W mass by fitting several high statistics simulated samples of different input masses which have been processed by exactly the same analysis procedure as the data. This generates a map from input mass to measured mass, which is inverted to convert the measured mass from data to the true W mass. The choice of function is motivated by the quality of the fit and sensitivity to shifts in the input mass.

Each invariant mass spectrum is fit seperately, since each channel has different mass resolution. The fit is realized as an unbinned maximum likelihood fit to the

average invariant mass distribution, where the probability for an event to have average invariant mass m is a combination of signal and background terms weighted by the purity of the selection:

$$\begin{aligned} L &= \prod_{i=1}^{N} P(m_i, \mathrm{M}) \\ P(m_i, \mathrm{M}) &= \Pi \cdot f_{\mathrm{signal}}(m_i, \mathrm{M}) + (1 - \Pi) \cdot f_{\mathrm{background}}(m_i) \end{aligned}$$

where Π is the purity, N is the number of events, and M is the estimator for $\mathrm{M_W}$. The signal term is a relativistic Breit Wigner with suppression of the form:

$$\begin{aligned} f_{\mathrm{signal}}(m, \mathrm{M}) &= A(\beta(1-\beta^2)) \cdot \left(\frac{2}{\pi} \frac{m^2 \Gamma}{(m^2 - \mathrm{M}^2)^2 + m^2 \Gamma^2} \right) \\ \beta &= \sqrt{1 - \frac{4m^2}{s}} \\ A &\Rightarrow \int f_{\mathrm{signal}}(m, \mathrm{M})\, dm = 1 \end{aligned}$$

The Γ parameter is determined by the natural width of the W and the resolution in invariant mass. Owing to the small size of the data samples, this parameter is fixed to the average of the simulated samples, making the fit a one parameter fit for M. The background term $f_{\mathrm{background}}$ is a background shape taken directly from the simulations of all expected sources weighted by cross section, and contains no information on the W mass.

The calibration samples for each channel are fit without background, producing a set of values $(M_{\mathrm{in}}^{\mathrm{MC}}, M_{\mathrm{out}}^{\mathrm{MC}})$. The deviation of $M_{\mathrm{out}}^{\mathrm{MC}}$ from $M_{\mathrm{in}}^{\mathrm{MC}}$, typically of order 500 MeV, arises from detector resolution effects, initial state radiation, and effects of the kinematic fit. This shift is taken as linear in input mass, with slope $a \sim 1$ and intercept b, determined from a least squares fit to the set of $(M_{\mathrm{in}}^{\mathrm{MC}}, M_{\mathrm{out}}^{\mathrm{MC}})$ values. Subsequently, the data distribution for that channel is fit with the same analytical function, but including background, and the result $M_{\mathrm{out}}^{\mathrm{D}}$ is converted to $\mathrm{M_W}$ and its

Channel	Slope	Intercept [GeV]	M_W [GeV]
$qqqq$	0.910 ± 0.021	7.98 ± 1.70	$80.75^{+0.53}_{-0.52}$
$qqe\nu$	0.989 ± 0.032	1.33 ± 2.61	$80.50^{+0.74}_{-0.73}$
$qq\mu\nu$	0.967 ± 0.037	3.20 ± 2.95	$80.91^{+1.11}_{-1.16}$
$qq\tau\nu$	0.981 ± 0.037	2.41 ± 3.21	$80.50^{+0.94}_{-1.08}$

Table 6: Results on M_W from the direct reconstruction method (Statistical errors only).

error δM_W by inverting the calibration function:

$$\begin{aligned} M_W &= \frac{(M^D_{out} - b)}{a} \\ (\delta M_W)^2 &= \frac{1}{a^2}\left((\delta a)^2 M_W^2 + (\delta b)^2 + (\delta M^D_{out})^2\right) \end{aligned}$$

The statistical error δM^D_{out} from the fit dominates the error from the calibration line parameters. Examples of calibration fits, calibration lines, and fits to the data are shown in figure 20 for the $qqe\nu$ channel and figure 21 for the $qqqq$ channel. The results for all channels are listed in table 6. The statistical errors agree with expected statistical errors given the size of the data samples.

Systematic errors

There are several uncertainties which give rise to systematic errors on M_W and need to be addressed. The first is the reliability of the fitting method, which is checked in several ways. The accuracy of the calibration line is tested by removing one calibration point from the parameter determination and treating it as data, thus comparing the measured "input mass" with the true input mass on a high statistics sample. This procedure reproduces the input mass to within the statistical errors of the sample. Additional systematic effects from the fitting method for each channel are assessed by changing the background shape and parametrization, and varying the fixed parameters of the fit, the purity and width, by their respective errors as determined from Monte Carlo studies. The systematic shift in the resulting output mass is evaluated on both the data and a set of 100 simulated experiments, which are event samples se-

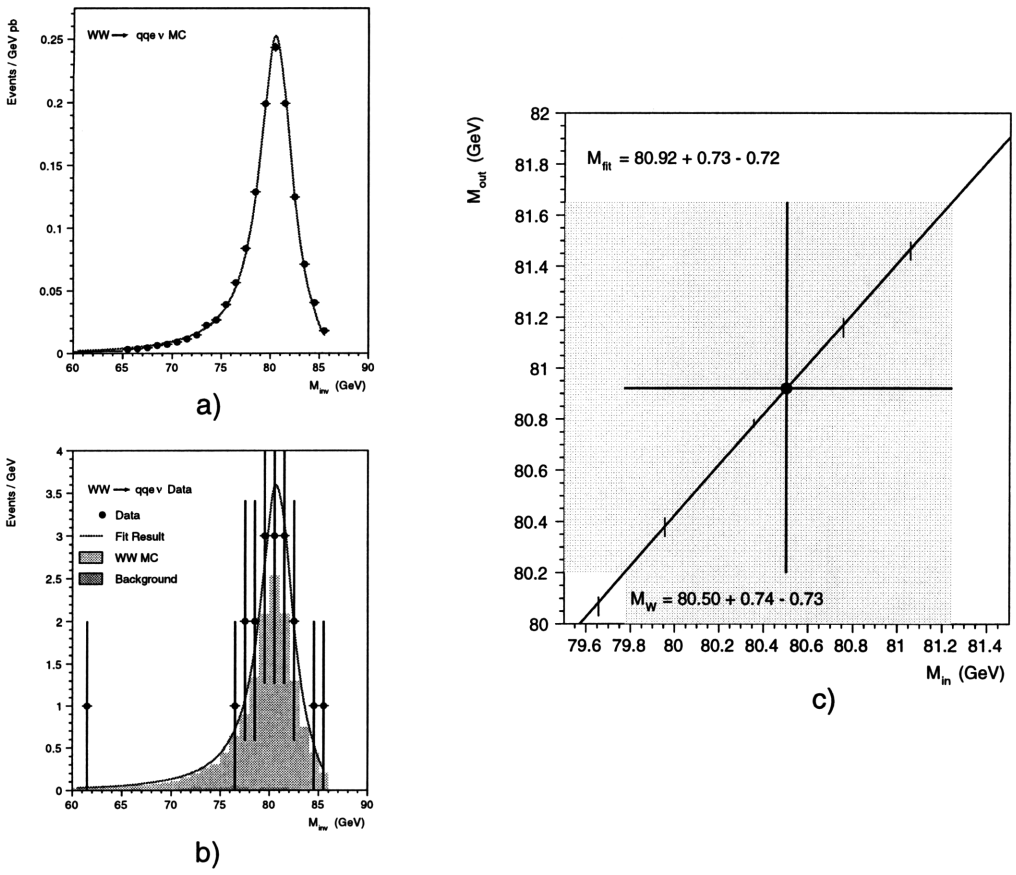

Figure 20: a) High statistics Monte Carlo fit, b) fit to the data, c) calibration line for the $qq\epsilon\nu$ channel.

lected from signal and background simulation according to the purity, with the same total number of events as the data. The results are tabulated in table 7.

Further systematic errors from the beam energy, detector effects and theoretical sources also need to be assessed. The use of the center of mass energy in determining the invariant mass spectra translates the LEP beam energy error of 30 MeV directly into a systematic error on M_W. Effects from missimulation of the measured energies and angles are assessed by fitting high statistics simulated samples where the energies and angles are varied within their resolutions before the kinematic fit. Theoretical errors associated with hadronization, higher order corrections, and initial state radiation are determined by fitting high statistics samples with different hadronization schemes and different inclusions of diagrams. The results are summarized in table 7, and in all cases are small compared to the statistical errors.

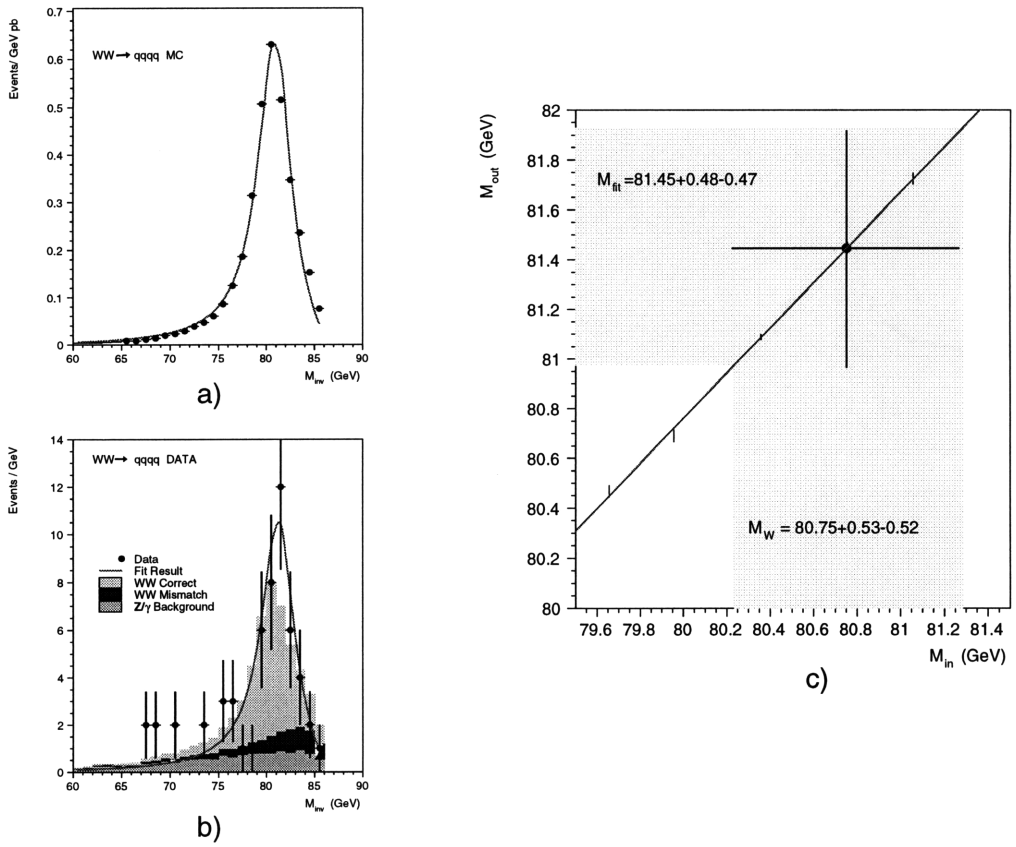

Figure 21: a) High statistics Monte Carlo fit, b) fit to the data, c) calibration line for the *qqqq* channel

6.3 Results

The consistency between the results from each individual channel (Table 6) allow the combination of the results in a simple weighted average, using the statistical errors as weights and the branching fractions to combine systematic errors, yielding:

$$M_W = 80.67 \pm 0.37 \pm 0.14 \text{ GeV}.$$

Contrasting this result from 10.25 pb^{-1} of data with the threshold method result $M_W = 80.82^{+0.44}_{-0.40} \pm 0.06$ from 11 pb^{-1} of data shows that the central values agree, and that direct reconstruction makes better use of the statistics available, but has higher systematics. As statistics still dominate the overall error and there is some room for systematic error improvement, direct reconstruction is advantageous for the best possible measurement of M_W, and will be pursued at yet higher center of mass

Systematic Errors on M_W [MeV]				
Source	Final State			
	$qqe\nu$	$qq\mu\nu$	$qq\tau\nu$	$qqqq$
$\sqrt{s}$	30	30	30	30
ISR	10	10	10	10
Hadronization	40	40	40	40
FSI (CR+BE)	—	—	—	100
Fitting Method	25	40	45	40
Background	30	15	45	65
Detector effects	50	30	10	20
Monte Carlo Statistics	40	40	40	40
Total	90	85	90	145

Table 7: Systematic errors in the determination of M_W for the different final states. The first three sources are treated as completely correlated for averaging purposes.

energies as LEPII continues (See Section 7.2). The results presented here can be combined for increased accuracy, giving as a final result:

$$M_W = 80.75 \pm 0.29 \text{ GeV}$$

7 Summary

7.1 Challenging the Standard Model

The work presented in the previous 6 sections represents the first measurements of the W-pair cross sections, W branching ratios and W mass to come from LEPII. In summary, the results are:

Observable	Experiment	Standard Model
$\sigma_{WW}(\sqrt{s} = 161$ GeV) [pb]	$2.87^{+0.80}_{-0.69} \pm 0.08$	3.87
$\sigma_{WW}(\sqrt{s} = 172$ GeV) [pb]	$12.12^{+1.43}_{-1.34} \pm 0.18$	12.41
$B(W \to qq)$[%]	$63.6^{+3.8}_{-4.0} \pm 0.4$	67.5
$B(W \to \ell\nu)$[%]	$12.1^{+1.3}_{-1.3} \pm 0.2$	10.8
M_W [GeV]	80.75 ± 0.29	80.352 ± 0.033

The results from these first measurements are consistent with the Standard Model predictions as well as all other measurements of the same quantities [20, 64–69] and support both the non-abelian nature of the theory and the assumption of lepton universality. Thus so far the Standard Model continues to show no signs of breakdown, and no new physics masquerading as W-pair production is evident.

The error on the mass measurement is roughly one order of magnitude larger than the error from the indirect measurements from LEPI data. Thus, the resulting additional sensitivity to the higgs mass when including this initial direct measurement of M_W is minimal (Table 2). Combining the results from all the LEP collaborations, all obtained in a manner similar to that of this thesis, the W Mass thus far from LEPII is [70]

$$M_W^{LEPII} = 80.48 \pm 0.13 \pm 0.04 \text{ GeV}$$

Comparison between electroweak fits using precision measurements including and omitting the M_W^{LEPII} measurement ([1] vs. [70]) provides an upper limit for the sensitivity of the higgs mass to the LEPII M_W measurement. Between these two analyses the

central value of the higgs mass is unchanged and the 1σ intervals change by roughly 10%. However, also included in this assessment are the updates to LEPI electroweak observables, so the influence of the M_W^{LEPII} measurement on the fit is presumably significantly less than even this small change. This conclusion is supported by the observation that the central value of M_W extracted from these analyses changes only by 20 MeV, and the error only by 6 MeV, after inclusion of the M_W^{LEPII} measurement.

The current situation in terms of electroweak corrections is illustrated in figure 22, which shows the 1σ contours of the direct and indirect determinations of M_W and m_t superimposed on the Standard Model predictions for $70 \leq m_H \leq 1000$ GeV. The intersection of the direct and indirect measurements seem to prefer low Higgs masses, but nothing conclusive is apparent. Thus, the progress to be made in the next few years is to continue the direct measurements and tighten the constraints on the Higgs mass.

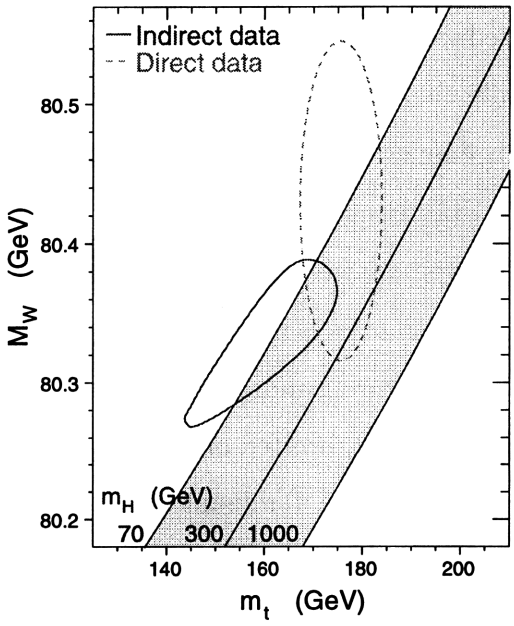

Figure 22: Comparison of direct and indirect measurements of M_W and m_t superimposed on the predicted band for $70 \leq m_H \leq 1000$ GeV [70].

7.2 Future Prospects

The LEPII physics program continues, already providing another ~ 55 pb^{-1} of data at $\sqrt{s} = 183$ GeV in 1997, with a target of 500 pb^{-1} above the W-pair threshold before terminating, resulting in a statistical error of 25-40 MeV on M_W. As all of the measurements are statistically limited, this is clearly the most effective way to improve these measurements. This data will provide accurate cross section measurements at several center of mass energies for further determination of the W-pair excitation curve and trilinear couplings, increase the accuracy of the branching ratio determinations by about one order of magnitude, and further refine the determination of M_W. Increased statistics will also allow competitive determinations of Γ_W and W polarization studies, which may provide an alternate avenue for probing the Higgs sector of the Standard Model [71].

With the statistical errors reduced by roughly one order of magnitude, the challenging task will be to reduce the systematic errors to this level, especially for the mass measurement. While there is no apparent "silver bullet" for the reduction of systematic errors, there is enough room for improvement on different fronts that the overall error can (perhaps) be reduced significantly.

Some reduction in the systematic error is almost guaranteed, as the means to reduce the error for particular sources is not difficult. The 30 MeV beam energy error will be reduced simply by performing more calibrations, the Monte Carlo statistics error can be made arbitrarily small, limited only by computer resources, and, as the center of mass energy is increased, the dominant backgrounds scale like s^{-1} while the W-pair cross sections increase or stay constant, so the signal to background conditions improve, though this improvement will be compensated by the increase in the other multiple boson production cross sections. Further reduction in the systematic errors is not so easily achieved, but the increase in data events should ameliorate the challenge somewhat, as systematic effects become clearly distinct from statistical fluctuations in the data, and measurements of effects from final state interactions reduce purely theoretical errors through input from experiment. Finally, more sophisticated fitting

methods can be used to reduce the fitting errors affecting the W mass measurement. For example, the use of more than one choice of pairing for the hadronic channel makes more efficient use of the mass information in the events, and different treatments of the background may reduce the systematics which stem from background uncertainties. Overall, though difficult, a significant reduction in the systematic errors of W-pair observables is certainly in the realm of possibility.

With this in mind, barring a discovery of new physics in this period, with 500 pb^{-1} of data and the methods outlined in this thesis, the direct measurement error on M_W will be of the same order as the indirect error, thus playing a significant role in the electroweak fits, which will tighten the constraints on the virtual contributions to the mass, indirectly exploring the Higgs sector and other contributions from new physics.

8 Acknowlegdements

I would like to thank the L3 Collaboration led by Professor S.C.C. Ting for the exemplary demonstration of collaboration in high energy physics. In particular, I am grateful to the members of the WW group, who have contributed much to this work and my education. Special thanks also goes to Professors Peter Fisher and Ulrich Becker, for their excellent advice and mentoring, and most of all to my wife and family, for the patient encouragement and support. I dedicate this thesis to them.

References

[1] The LEP Collaborations, ALEPH, DELPHI, L3, OPAL and the LEP Electroweak Working Group, A Combination of Preliminary LEP Electroweak Measurements and Constraints on the Standard Model, Preprint CERN-PPE/96-183, CERN, 1996.

[2] E. Fermi, Z. Phys. **88** (1934) 161.

[3] I. Curie and F. Joliot, C.R. Acad. Sci. **198** (1934) 48.

[4] Lee, T.D. and C.N. Yang, Phys. Rev. **104** (1956) 1254.

[5] C.S. Wu *et al.*, Phys. Rev. **105** (1957) 1413.

[6] W. Heisenberg, Z. Phys. **101** (1936) 533.

[7] S.L. Glashow, Nucl. Phys. **22** (1961) 579.

[8] A. Salam, in Elementary Particle Theory, ed. N. Svartholm, (Almqvist and Wiksell, Stockholm, 1968), p. 367.

[9] S. Weinberg, Phys. Rev. Lett. **19** (1967) 1264.

[10] F. Halzen and A.D. Martin, Quarks and Leptons: An Introductory Course in Modern Particle Physics, (John Wiley and Sons, New York, 1984).

[11] E.D Commins and P.H. Bucksbaum, Weak interactions of leptons and quarks, (Cambridge University Press, Cambridge, 1983).

[12] P. W. Higgs, Phys. Lett. **12** (1964) 132, Phys. Rev. Lett. **13** (1964) 508 and Phys. Rev. **145** (1966) 1156;
F. Englert and R. Brout, Phys. Rev. Lett. **13** (1964) 321..

[13] G. 't Hooft, Nucl. Phys. **B 35** (1971) 21.

[14] Gargamelle Collab., F.J. Hasert *et al.*, Phys. Lett. **46 B** (1973) 121.

[15] C.Y. Prescott *et al.*, Phys. Lett. **77 B** (1978) 347.

[16] UA1 Collab., G. Arnison *et al.*, Phys. Lett. **122 B** (1983) 103.

[17] UA2 Collab., M. Banner *et al.*, Phys. Lett. **122 B** (1983) 476.

[18] UA1 Collab., G. Arnison *et al.*, Phys. Lett. **126 B** (1983) 398.

[19] UA2 Collab., P. Bagnaia *et al.*, Phys. Lett. **129 B** (1983) 130.

[20] M. Rijssenbeek, *Measurements of the Mass of the W Boson from CDF/DØ*, to appear in the proceedings of the 28th International Conference on High Energy Physics, 25-31 July 1996, Warsaw, Poland.

[21] DØ Collab., S. Abachi *et al.*, Phys. Rev. Lett. **79** (1997) 1197.

[22] DØ Collab., S. Abachi *et al.*, *Measurement of the Top Quark Mass Using Dilepton Events*, Preprint FERMILAB-PUB-97/172-E, FERMILAB, 1997.

[23] CDF Collab., F. Abe *et al.*, *Measurement of the Top Quark Mass*, Preprint FERMILAB-PUB-97/352-E, FERMILAB, 1997.

[24] CDF Collab., F. Abe *et al.*, *Measurement of the Top Quark Mass and $t\bar{t}$ Production Cross Section from Dilepton Events at the Collider Detector at Fermilab*, Preprint FERMILAB-PUB-97/304-E, FERMILAB, 1997.

[25] W. Alles, Ch. Boyer, and A.J. Buras, Nucl. Phys. **B 119** (1977) 125.

[26] W. Beenakker *et al.*, in *Physics at LEP 2*, Report CERN 96-01 (1996), eds G. Altarelli, T. Sjöstrand, F. Zwirner, Vol. 1, p. 79.

[27] D. Bardin *et al.*, Nucl. Phys. (Proc. Suppl.) **B 37** (1994) 148;
F.A. Berends *et al.*, Nucl. Phys. (Proc. Suppl.) **B 37** (1994) 163.

[28] N. Cabibbo, Phys. Rev. Lett. **10** (1963) 531;
M. Kobayashi and T. Maskawa, Prog. Theor. Phys. **49** (1973) 652.

[29] R.M. Barnett *et al.*, *Review of Particle Properties*, Phys. Rev. **D 54** (1996) 94; and references therein.

[30] D.C. Kennedy and B.W. Lynn, Phys. Lett. **B 322** (1989) 54.

[31] M.E. Peskin and T. Takeuchi, Phys. Rev. **D 46** (1992) 381.

[32] G. Burgers and F. Jegerlehner, in *Z Physics at LEP 1*, CERN Report CERN 89-08, eds G. Altarelli,R. Kleiss and C. Verzegnassi (CERN, Geneva, 1989) Vol. 1, p. 55.

[33] Z. Kunszt *et al.*, in *Physics at LEP 2*, Report CERN 96-01 (1996), eds G. Altarelli, T. Sjöstrand, F. Zwirner, Vol. 1, p. 141.

[34] G. Gustafson, U. Petterson and P.M. Zerwas, Phys. Lett. **B 209** (1988) 90;
T. Sjöstrand and V.A. Khoze, Z. Phys. **C 62** (1994) 281, Phys. Rev. Lett. **72** (1994) 28;
E. Accomando, A. Ballestrero and E. Maina, Phys. Lett. **B 362** (1995) 141;
G. Gustaffson and J. Häkkinen, Z. Phys. **C 64** (1994) 659;
L. Lönnblad, Z. Phys. **C 70** (1996) 107;
J. Ellis and K. Geiger, Phys. Rev. **D 54** (1996) 1967, *Signatures of Parton Exogamy in* $e^+e^- \to W^+W^- \to$ *hadrons*, CERN-TH/97-046.

[35] L. Lönnblad and T. Sjöstrand, Phys. Lett. **B 351** (1995) 293;
S. Jadach and K. Zalewski, *W Mass Reconstruction from Hadronic Events in LEP-2: Bose Einstein Effect*, CERN-TH/97-029.

[36] LEP Injector Study Group, *LEP Design Report*, volume 1, (CERN, Geneva, 1983).

[37] LEP Main Ring Study Group, *LEP Design Report*, volume 2, (CERN, Geneva, 1984).

[38] LEP2 Team, *LEP Design Report*, volume 3, (CERN, Geneva, 1996).

[39] S. Myers and C. Wyss, in *Physics at LEP 2*, Report CERN 96-01 (1996), eds G. Altarelli, T. Sjöstrand, F. Zwirner, Vol. 1, p. 23.

[40] LEP Polarization Collab., L. Arnaudon *et al.*, Phys. Lett. **B 284** (1992) 431.

[41] V. Bargmann, L. Michel, and V.L. Telegdi, Phys. Rev. Lett. **2** (1959) 435.

[42] R.M. Barnett *et al.*, *Review of Particle Properties*, Phys. Rev. **D 54** (1996) 1; and references therein.

[43] Working Group on LEP Energy and the LEP Collaborations ALEPH, DELPHI, L3 and OPAL, L. Arnaudon *et al.*, Phys. Lett. **B 307** (1993) 187.

[44] A. Blondel *et al.*, in *Proceedings from the 1997 Particle Accelerator Conference*, (TRIUMF, Vancouver, 1997).

[45] The L3 Collab., B. Adeva *et al.*, Nucl. Instr. and Meth. **A 289** (1990) 35;
M. Chemarin *et al.*, Nucl. Instr. and Meth. **A 349** (1994) 345;
M. Acciarri *et al.*, Nucl. Instr. and Meth. **A 351** (1994) 300;
I.C. Brock *et al.*, Nucl. Instr. and Meth. **A 381** (1996) 236;
A. Adam *et al.*, Nucl. Instr. and Meth. **A 383** (1996) 342.

[46] A. Adam *et al.*, *The Forward Muon Detector of L3*, CERN-PPE/96-97.

[47] I.C. Brock *et al.*, Nucl. Instr. and Meth. **A 381** (1996) 236.

[48] Particle Data Group: R.M. Barnett *et al.*, Phys. Rev. **D 54** (1996) 168.

[49] The KORALW version 1.21 is used.
M. Skrzypek, S. Jadach, W. Placzek and Z. Wąs, Comp. Phys. Comm. **94** (1996) 216;
M. Skrzypek, S. Jadach, M. Martinez, W. Placzek and Z. Wąs, Phys. Lett. **B 372** (1996) 289.

[50] F.A. Berends, R. Kleiss and R. Pittau, Nucl. Phys. **B 424** (1994) 308; Nucl. Phys. **B 426** (1994) 344; Nucl. Phys. (Proc. Suppl.) **B 37** (1994) 163;

R. Kleiss and R. Pittau, Comp. Phys. Comm. **83** (1994) 141;
R. Pittau, Phys. Lett. **B 335** (1994) 490.

[51] T. Sjöstrand, *PYTHIA 5.7 and JETSET 7.4 Physics and Manual*, CERN-TH/7112/93 (1993), revised August 1995; Comp. Phys. Comm. **82** (1994) 74.

[52] The L3 detector simulation is based on GEANT Version 3.15.
R. Brun *et al.*, "GEANT 3", CERN DD/EE/84-1 (Revised), September 1987.
The GHEISHA program (H. Fesefeldt, RWTH Aachen Report PITHA 85/02 (1985)) is used to simulate hadronic interactions..

[53] L3 Collab., M. Acciarri *et al.*, Phys. Lett. **B 407** (1997) 389.

[54] The working group on LEP energy, *LEP Energy Calibration in 1996*, LEP Energy Group/97-01.

[55] L3 Collab., M. Acciarri *et al.*, Phys. Lett. **B 398** (1997) 223.

[56] L3 Collab., M. Acciarri *et al.*, Phys. Lett. **B 407** (1997) 419.

[57] F. Boudjema *et al.*, in *Physics at LEP 2*, Report CERN 96-01 (1996), eds G. Altarelli, T. Sjöstrand, F. Zwirner, Vol. 1, p. 209.

[58] S. Catani *et al.*, Phys. Lett. **B 269** (1991) 432;
S. Bethke *et al.*, Nucl. Phys. **B 370** (1992) 310.

[59] C. Peterson *et al.*, Comp. Phys. Comm. **81** (1994) 185.

[60] The L3 Collab., M. Acciarri *et al.*, *Measurements of Mass, Width and Gauge Couplings of the W Boson at LEP*, CERN-PPE/97-98.

[61] The GENTLE version 2.0 is used.
D. Bardin *et al.*, *GENTLE/4fan v. 2.0: A Program for the Semi-Analytic Calculation of Predictions for the Process* $e^+e^- \to 4f$, DESY 96-233, hep-ph/9612409.

[62] The UA1 Collab., C. Albajar *et al.*, Phys. Lett. **B 253** (1991) 503;
The UA2 Collab., J. Alitti *et al.*, Phys. Lett. **B 276** (1992) 365;
The CDF Collab., F. Abe *et al.*, Phys. Rev. Lett. **74** (1995) 341; Phys. Rev. **D 52** (1995) 2624;
The DØ Collab., S .Abachi *et al.*, Phys. Rev. Lett. **75** (1995) 1456.
We use the average value and error for the total width of the W boson as listed in:
R.M. Barnett *et al.*, *Review of Particle Properties*, Phys. Rev. **D 54** (1996) 1.

[63] D. Bardin *et al.*, in *Physics at LEP 2*, Report CERN 96-01 (1996), eds G. Altarelli, T. Sjöstrand, F. Zwirner, Vol. 2, p. 3.

[64] The OPAL Collab., K. Ackerstaff *et al.*, Phys. Lett. **B 389** (1996) 416.

[65] The ALEPH Collab., R. Barate *et al.*, Phys. Lett. **B 401** (1997) 347.

[66] The DELPHI Collab., P. Abreu *et al.*, Phys. Lett. **B 397** (1997) 158.

[67] The OPAL Collab., K. Ackerstaff *et al.*, Measurement of the W Boson Mass and W^+W^- Production and Decay Properties in e^+e^- Collisions at $\sqrt{s} = 172$ GeV, Preprint CERN-PPE/97-116, CERN, 1997.

[68] The DELPHI Collab., P. Abreu *et al.*, Measurement of the W-pair cross-section and of the W Mass in e^+e^- interactions at 172 GeV, Preprint CERN-PPE/97-160, CERN, 1997.

[69] The ALEPH Collab., R. Barate *et al.*, Measurement of the W-pair cross sections in e^+e^- collisions at 172 GeV, Preprint CERN-PPE/97-102, CERN, 1997.

[70] The LEP Collaborations, ALEPH, DELPHI, L3, OPAL and the LEP Electroweak Working Group, and the SLD Heavy Flavor Group, A Combination of Preliminary LEP Electroweak Measurements and Constraints on the Standard Model, Preprint CERN-PPE/97-154, CERN, 1997.

[71] B.W. Lee, C. Quigg, and H.B. Thacker, Phys. Rev. **D 16** (1977) 1519.